USING NONLINEAR ULTRASOUND MEASUREMENTS TO ASSESS THE STAGE OF THERMAL DAMAGE IN MODIFIED 9%CR FERRITIC MARTENSITIC STEEL

A Thesis
Presented to
The Academic Faculty

by

Daniel Marino

In Partial Fulfillment
of the Requirements for the Degree
Master of Science in Engineering Science and Mechanics in the
School of Civil and Environmental Engineering

Georgia Institute of Technology
December 2014

USING NONLINEAR ULTRASOUND MEASUREMENTS TO ASSESS THE STAGE OF THERMAL DAMAGE IN MODIFIED 9%CR FERRITIC MARTENSITIC STEEL

Approved by:

Professor Laurence J. Jacobs, Advisor
School of Civil and Environmental Engineering
Georgia Institute of Technology

Dr. Jin-Yeon Kim
School of Civil and Environmental Engineering
Georgia Institute of Technology

Dr. Jianmin Qu
Department of Civil and Environmental Engineering
Northwestern University

Date Approved: 22 August 2014

ACKNOWLEDGEMENTS

First of all, I want to thank my advisor Professor Laurence J. Jacobs for his support and the motivation throughout my graduate studies at Georgia Tech. Apart from giving me the opportunity to come to Atlanta, he always helped me with all sorts of problems and he made it possible to participate and present my work at the quantitative nondestructive evaluation (QNDE) conference in Boise, ID.

I also would like to acknowledge Dr. Jin-Yeon Kim for his excellent practical and professional help in the field of nondestructive evaluation. He supported me in this research and made it possible to write this thesis.

I also want to thank Dr. Jianmin Qu from Northwestern University for reviewing my thesis and serving as a committee member.

I also want to thank Dr. Alberto Ruiz from Instituto de Investigaciones Metalurgicas in Morelia, Mexico, for conducting complimentary measurements including scanning electron microscopy and Rockwell HRC hardness tests, and Dr. Young-Sang Joo from Korea Atomic Energy Institute for providing specimens and helpful comments.

Further thanks go to my lab mates Katie Matlack, Anne Romer, David Torello, Florian Morlock and Gun Kim making the time in the lab interesting, informative and from time to time entertaining. Special thanks thereby goes to Anne Romer and Florian Morlock for sharing joy and sorrow with me during our stay in Atlanta.

I also want to thank Prof. Lothar Gaul, Sibylle Langer and Christian Ehrlich from University of Stuttgart for choosing me as a candidate for the ISAP program, which is financially supported by the DAAD.

Last but not least, I thank my family and all my friends in Germany for supporting me throughout my time at Georgia Tech.

TABLE OF CONTENTS

LIST OF TABLES

LIST OF FIGURES

LIST OF SYMBOLS OR ABBREVIATIONS

Symbol	Description
a_s	source radius
A_n	wave amplitude
A_n^{el}	detected electrical amplitude of a wave
A_e, B_e	Huang coefficients
b_i	body force
A_i, B_i	amplitudes
$\vec{b}$	Burger's vector
c	wave velocity
c_D, c_S, c_R	longitudinal, transverse, Rayleigh wave velocity
C_1	initial stress
C_{ijkl}	fourth order elastic tensor
C_{ijklmn}, M_{ijklmn}	higher order elastic tensor
ds	line segment
$\vec{d}$	unit particle vector
E	Young's modulus
f	angular frequency
f_p	volume fraction precipitates
F	force
F_{obs}	force of an obstacle
G	shear modulus
i	imaginary unit
k_n	wavenumber
k_L, k_R	longitudinal, Rayleigh wavenumber
l_{off}	lift off distance
K	bulk modulus precipitate

Symbol	Description
n_j	unit normal vector
$\vec{p}$	unit propagation vector
P, Q	second and higher elastic constants
R	conversion factor longitudinal-shear stress
r	radius of the bowed dislocation
r_p	radius precipitates
r_0	initial radius precipitate
S	surface
S_d	area swept out by a dislocation
t	time
t_s	specimen thickness
T	dislocation line tension
t_i	traction on surface
u_i	displacement
$\vec{u}$	displacement vector
u_i	displacement
$\ddot{u}_i$	acceleration
V	volume
$\vec{x}, x_i$	Lagrangian coordinates
W	specific strain energy
x_1	propagation direction
x_3	direction into finite half space
$2L$	pinning distance dislocation line
α_n	attenuation coefficient
β	nonlinearity parameter
β'	relative nonlinearity parameter
β^{lat}	nonlinearity parameter due to lattice nonlinearity
β^{disloc}	nonlinear contribution of dislocation network

Symbol	Description
γ_d	shear strain
δ	misfit parameter
δ_{ij}	Kronecker delta
ϵ	total strain
ϵ_e	elastic strain
ϵ_d	strain caused by dislocations
ϵ_{ij}	strain tensor
ε	actual misfit parameter
θ_i	incident/reflection/transmission angle
θ_D, θ_R	angle of longitudinal, Rayleigh wave
θ_w	angle of the plexiglas wedge
λ, μ	Lamé constants
λ	wavelength
Λ_R	Rayleigh wavelength
$\Lambda^{(d)}$	dislocation density
ν	Poisson's ratio
ρ	material mass density
σ	longitudinal stress
σ_{ij}	Cauchy stress tensor
σ_{Orowan}	Orowan stress
τ	shear stress
τ_d	shear stress on dislocation
Φ	scalar potential
Φ_c	critical angle of dislocation to overcome obstacle
$\varphi_{n,0}$	phase
$\vec{\Psi}$	vector potential
ω	circular frequency
Ω	conversion factor shear-longitudinal strain

SUMMARY

This research investigates second harmonic generation in Rayleigh surface waves propagating in 9%Cr ferritic martensitic steel. Previous experimental results show that the nonlinearity parameter is sensitive to certain changes in a material's properties such as thermal embrittlement and hardness changes. Therefore, the nonlinearity parameter can be used as an indicator of thermal damage due to changes in dislocation density and precipitations. The specimens are isothermally aged for different holding times to create progressive changes in the microstructure and obtain different levels of thermal aging damage. As aging progresses the dislocation density decreases and precipitations are formed; these microstructural evolutions lead to changes in the nonlinearity parameter β. Nonlinear ultrasonic experiments are conducted for each specimen using a wedge transducer for generation and an air-coupled transducer for detection of Rayleigh surface waves. The amplitudes of the first and second order harmonics are measured at different propagation distances, and these amplitudes are used to obtain the relative nonlinearity parameter for each specimen at different aging stages. Conclusions about microstructural changes are drawn based on the nonlinear Rayleigh surface wave measurement and complementary measurements including scanning electron microscopy (SEM) and Rockwell HRC hardness. The results indicate that the nonlinearity parameter is very sensitive to the dislocation density and precipitate formation, and thus can be used to track the microstructural change in this material during the process of thermal aging.

CHAPTER I

INTRODUCTION

1.1 Motivation and Objectives

Thermal aging of ferritic martensitic steel at temperatures of 600°C and higher can pose a high risk to components such as piping, turbines or steam vessels because of drops in the mechanical properties of the steel such as strength or creep resistance. This unexpected drop can lead to a dramatic failure during long-term operation.

Modified 9%Cr steel is a common material used in the power generation, chemical and petroleum industries. Especially in the power generation industry, 9%Cr steel is an attractive solution to handle the high temperature and pressure since it provides a sufficient strength, resistance to corrosion and oxidation, low thermal expansion and adequate fatigue resistance. Furthermore, it is relatively cheap compared to other materials such as austenitic stainless steels, which are capable of satisfying the same requirements [16]. For this reason, 9%Cr steel is an effective trade-off to balance cost and high temperature. However, an increased demand to improve the efficiency of power plants requires an exposure to higher temperatures and pressures. The higher operating conditions (temperature about 650°C) need a careful consideration of the degradation mechanisms that occur during thermal aging.

The elevated temperature changes the microstructure since various precipitations respond differently to altering environmental conditions. The changing microstructure and an accelerating dissolution of lath martensite that contains a high amount of dislocations cause a degradation of the steel's mechanical properties. Nonlinear nondestructive evaluation techniques are preferred over conventional linear ultrasonic measurements because of their ability to detect microstructural changes prior to significant drops in strength and failure.

Hikata et al. [14] derived a relationship between the pinning of dislocations and the generation of a second harmonic component. This study was extended by Cantrell et al. [3] by considering the stress field introduced by precipitates, which pins dislocations. The findings of these studies and further experiments ([20], [24], [27], [31], etc.) based on these results justify the use of nonlinear ultrasound to investigate the change in the microstructure due to thermal aging.

Rayleigh surface waves used in this research have some ideal features for nondestructive evaluation since they have the natural ability to travel a longer propagation distance due to less spreading, compared to bulk and shear waves. Furthermore, Rayleigh waves only require single-sided access, making them particularly interesting for field application.

The objective of this research is to develop a non-contact detection method to track changes in the microstructure of 9%Cr steel based on nonlinear Rayleigh waves with varying propagation distances. With the help of the measured nonlinearity parameter β, we experimentally assess the stage of thermal damage for each sample. Once this objective is achieved, complementary measurements (hardness tests, metallurgical analyses) are performed to provide information on the mechanical properties and microstructure of the aged steel, to complement the nonlinear ultrasonic results obtained and to help interpret the trends observed in the measured β values.

1.2 Structure of the Thesis

Chapter 2 is a brief introduction to the basics of linear wave propagation in solid media and characteristics of Rayleigh waves, followed by the derivation of the nonlinearity parameter β in terms of the measurable out-of-plane displacement.

In a next step, chapter 3 describes the production, chemical composition and geometry of the modified 9%Cr steel samples investigated in this research.

After the chapter on the material, chapter 4 describes briefly the performed heat treatment schedule to obtain six samples in a different stage of thermal aging (holding times of $0h, 200h, 500h, 1000h, 1500h$ and $3000h$). Subsequently, the mechanisms during thermal aging are described in detail, namely: (i) nucleation, growth and coarsening of precipitates;

(ii) dislocations and their interaction with precipitates; (iii) evolution of precipitates in modified 9%Cr steel. Finally, the chapter shows the theoretical approach to explain the contribution of microstructural changes on the nonlinearity parameter β.

Chapter 5 gives a brief overview on the setup and the components to measure Rayleigh waves with an air-coupled transducer, followed by the necessary assumptions to process the ultrasonic datas. Moreover, the chapter explains the procedure to perform the measurements, which consists of determining the path of the acoustic beam and the actual measurement along the propagation direction.

Chapter 6 evaluates the results of the complementary tests and the nonlinear measurement and interprets the findings. Based on this interpretation, chapter 7 draws a conclusion and gives an outlook for subsequent work.

CHAPTER II

WAVE PROPAGATION IN SOLIDS

Wave propagation in elastic solids provides a useful tool in mechanical engineering to conduct nondestructive tests since the propagating wave interacts with microstructural changes and macroscopic defects. This chapter discusses the fundamentals of wave propagation in solid materials. On this basis, the Rayleigh wave is introduced as a special wave that can propagate along a stress-free surface of an elastic half space. The last step focuses on wave propagation in an elastic homogeneous material with a nonlinear stress-strain relationship. Based on this relationship the nonlinearity parameter is defined as an indicator of the material nonlinearity. Further down it is shown that the nonlinearity correlates with the state of thermal aging.

2.1 Wave Equation in Linear Elastic Solids

The propagation of waves in an unbounded medium can be derived by using the equation of momentum and compatibility. Furthermore, the constitutive relationship is necessary to connect applied stresses or forces to strains or deformations. The derivation is in conformity with Achenbach [1].

The balance of linear momentum for a body of volume V and surface S is given by

$$\int_S t_i \mathrm{d}S + \int_V b_i \mathrm{d}V = \int_V \rho \ddot{u}_i \mathrm{d}V \tag{1}$$

Here ρ denotes the material mass density, b_i represents the body force, t_i is the traction on the surface S and $\ddot{u}_i$ represents the second derivative of the displacement u_i with respect to time. If the Cauchy stress formula

$$t_i = n_j \sigma_{ij} \tag{2}$$

with σ_{ij} as the Cauchy stress is substituted in equation (1) and the Gauss' theorem is applied to transform the surface integral into a volume integral

$$\int_V \rho \frac{\partial^2 u_i}{\partial t^2} dV = \int_V \partial_j \sigma_{ij} dV + \int_V b_i dV \tag{3}$$

is obtained. Since the volume V is arbitrary and equation (3) has to be valid for any volume V, the localization argument can be used. This results in Cauchy's equation, also known as linear momentum equation.

linear momentum equation

$$\rho \frac{\partial^2 u_i}{\partial t^2} = \partial_j \sigma_{ij} + b_i \tag{4}$$

Equation (5) gives the relationship between the strain ϵ_{ij} and the displacement u_i.

compatibility equation

$$\epsilon_{ij} = \frac{1}{2}(\partial_i u_j + \partial_j u_i) \tag{5}$$

To derive the wave equation the constitutive relationship is the last necessary equation. It connects applied stresses or forces to strains or deformations. In general, the relationship between the stress σ_{ij} and strain ϵ_{kl} tensor is given by the fourth order stiffness tensor C_{ijkl} by

$$\sigma_{ij} = C_{ijkl}\epsilon_{kl} \tag{6}$$

C_{ijkl} contains the mechanical properties of the material. Since it is assumed that the material is a linearly elastic, isotropic and homogeneous solid, the coefficients of C_{ijkl} are constant and can be described in terms of the Lamé constants λ and μ . Equation (7) is the known Hooke's Law in the three dimensional space.

constitutive relationship

$$\sigma_{ij} = \lambda \epsilon_{kk} \delta ij + 2\epsilon_{ij} \tag{7}$$

The Lamé elastic constants can be denoted by the material properties Young's modulus E and Poisson's ratio ν. They are related by

$$\lambda = \frac{E\nu}{(1+\nu)(1-2\nu)} \tag{8}$$

$$\mu = \frac{E}{2(1+\nu)} \tag{9}$$

The wave equation expressed in index notation can be obtained by using equation (4), (5) and (7) and the simplification $\nabla\lambda = 0$ and $\nabla\mu = 0$. The spatial variation of the Lamé constants λ and μ can be neglected in a homogeneous material. Furthermore, the body

force b_i in the momentum equation is neglected.

$$\rho\frac{\partial^2\vec{u}}{\partial t^2} = (\lambda+\mu)\nabla\nabla\cdot\vec{u} + \mu\nabla^2\vec{u} \tag{10}$$

Equation (10) represents a set of coupled partial differential equations which can be uncoupled by using the vector identity $-\nabla\times\nabla\times\vec{u} + \nabla\nabla\cdot\vec{u} = \nabla^2\vec{u}$. Thus, equation (10) can be obtained in terms of

$$\rho\frac{\partial^2\vec{u}}{\partial t^2} = (\lambda+2\mu)\nabla\nabla\cdot\vec{u} - \mu\nabla\times\nabla\times\vec{u} \tag{11}$$

By applying the vector identity, it is possible to separate the equation into a solution for a compression wave (P-wave) and a shear wave (SV-wave). The solution of equation (11) can be written as the Helmholtz decomposition

$$\vec{u} = \nabla\Phi + \nabla\times\vec{\Psi} \tag{12}$$

where the displacement $\vec{u}$ is represented by the four functions Φ, Ψ_1, Ψ_2 and Ψ_3. To guarantee uniqueness of the solution an additional constraint $\nabla\cdot\Phi = 0$ is necessary. This approach was introduced by Helmholtz and enables the study of partial differential equations in both space and time. In our case, the Helmholtz decomposition uses the gradient of the scalar Φ and the curl of the zero-divergence vector potential $\vec{\Psi}$ to separate the compression and shear wave. This is only applicable because the whole derivation works in the linear regime and the principle of superposition is valid.

To show that the Helmholtz decomposition leads to the uncoupled partial differential equations, the divergence is applied to equation (11). Equation (12) can be solved for the compression wave by using the mathematical identity $\nabla\cdot(\nabla\times\vec{x}) = 0$.

$$\rho\frac{\partial^2(\nabla\vec{u})}{\partial t^2} = (\lambda+2\mu)\nabla^2(\nabla\cdot\vec{u}) \tag{13}$$

By substituting $\Phi = \nabla\cdot\vec{u}$ the first wave equation can be written in terms of

$$\nabla^2\Phi - \frac{1}{c_D^2}\frac{\partial^2}{\partial t^2}\Phi = 0 \tag{14}$$

with the phase velocity of the compression wave

$$c_D = \sqrt{\frac{\lambda+2\mu}{\rho}} \tag{15}$$

By taking the curl of equation (11) and using the identity that $\nabla \times \Phi = 0$ for any scalar Φ.

$$\rho \frac{\partial^2 (\nabla \times \vec{u})}{\partial t^2} = \mu \nabla^2 (\nabla \times \vec{u}) \tag{16}$$

The substitution $\vec{\Psi} = \nabla \times \vec{u}$ simplifies the equation to the second wave equation

$$\nabla^2 \vec{\Psi} - \frac{1}{c_S^2} \frac{\partial^2}{\partial t^2} \vec{\Psi} = 0 \tag{17}$$

with the phase velocity of the shear wave

$$c_S = \sqrt{\frac{\mu}{\rho}} \tag{18}$$

It can be shown that Φ and $\vec{\Psi}$ are solutions of the two uncoupled wave equations. The first equation is for a compression (also called dilatational, irrotational, pressure wave or P-wave) and the second for a shear (also called transverse, rotational, distortional wave or S-wave) wave. Furthermore, since both phase velocities have only a dependence on the material mass density ρ and the Lamé constants λ and μ, it can be concluded that for any material $c_D > c_S$.

2.2 Wave Phenomena

2.2.1 Plane Wave Propagation

This section considers a plane wave in an infinite media. The assumption of a plane wave implies a wave of constant frequency f and amplitude A with wavefronts which are considered as an infinitely long straight line. The propagation direction $\vec{p}$ is perpendicular to the wavefront. The mathematical representation is given by

$$\vec{u} = \vec{d} f(\vec{x} \cdot \vec{p} - ct) \tag{19}$$

where c represents either the longitudinal or shear phase velocity c_D or c_S, respectively. Furthermore, vector $\vec{d}$ denotes the direction of the particle movement, also called the displacement vector. By substituting equation (19) into (11), we obtain

$$(\mu - \rho c^2)\vec{d} + (\lambda + \mu)(\vec{p} \cdot \vec{d})\vec{p} = 0 \tag{20}$$

Since $\vec{p}$ and $\vec{d}$ are different unit vectors, there are only two possible solutions to satisfy the equation.

1. $\vec{d} = \pm\vec{p}$: this implies that $\vec{p} \cdot \vec{d} = 1$; the particle displacement is in the same direction as the propagating wave and equation (20) yields $c = c_D$ as shown in equation (15)

2. $\vec{p} \cdot \vec{d} = 0$: this solution denotes a shear wave, since the motion of particles is perpendicular to the propagation direction. Solving equation (20) leads to $c = c_S$, as defined in equation (18)

2.2.2 Harmonic Waves

Harmonic waves represent a special form of plane waves travelling with phase velocity c and their direction is given by the unit vector $\vec{p}$. The function can be written as

$$f(\vec{x} \cdot \vec{p} - ct) = e^{ik(\vec{x} \cdot \vec{p} - ct)} \tag{21}$$

where k stands for the wavenumber and is defined as $k = \frac{\omega}{c} = \frac{2\pi}{\lambda}$. With a given amplitude A, which is independent of time t and position $\vec{x}$, we can define the displacement field expression for a general time harmonic wave

$$\vec{u}^{(n)} = A_n \vec{d}^{(n)} e^{ik_n(\vec{x} \cdot \vec{p}^{(n)} - c_n t)} \tag{22}$$

with n denoting the wave type i.e. longitudinal (D) or shear wave (S).

2.2.3 Reflection on Stress-Free Surface

The above derived wave types independently propagate in an infinite medium. However, nearly every application of ultrasound involves the interaction of waves with boundaries. As soon as a finite medium is considered, boundaries between media generate reflection and transmission. The general case of a boundary between two media can be found in [25].

In the further discussion, we only consider the idealized case of a boundary between a medium and vacuum (e.g. idealized air). This coupling describes a stress-free surface without transmission.

The following figure 2.1 shows an example of an incident P- and SV-wave with the incident angle θ_0 and their reflected waves with the angles θ_1 and θ_2 for the reflected P- and SV-wave. Both incident waves propagate in the x_1x_3-plane, with the boundary perpendicular to the x_3-axis. The resulting conditions for a stress-free boundary are $\tau_{33} = 0$ and $\tau_{31} = 0$, which are used to derive Rayleigh waves.

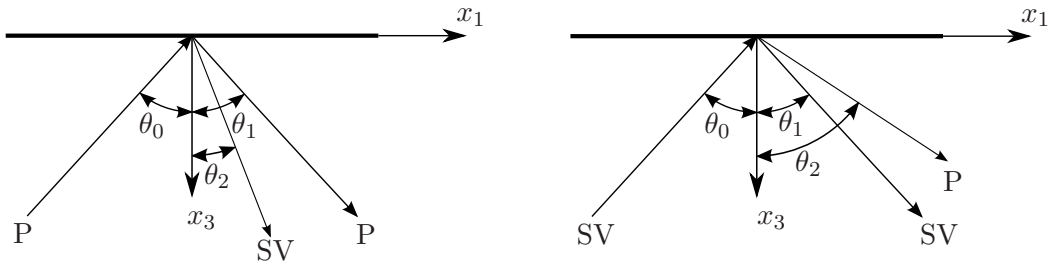

Figure 2.1: Reflection of P-wave and SV-wave

Using equation (22) and the fact that ω does not change after the reflection, it is possible to identify a correlation between the angles θ_0, θ_1 and θ_2. To obtain a non-trivial solution for the amplitudes A_n (here n=1, 2, 3), the angles have to satisfy Snell's law

$$k_0 sin(\theta_0) = k_1 sin(\theta_1) = k_2 sin(\theta_2) \tag{23}$$

2.2.4 Generation of Rayleigh Waves

The generation of Rayleigh waves is achieved by a longitudinal ultrasonic transducer attached to a wedge-shaped body. Refraction in the boundary between the wedge and the specimen creates the desired Rayleigh wave. The shape of the wedge, especially the angle of the impinging wave (θ_1), is crucial for the generation, as depicted in figure 2.2.

Again we can use Snell's law (23) expressed in terms of the wave velocities ($c_1 = c_D$ and $c_2 = c_R$) to determine the angle $\theta_1 = \theta_D$. Since the Rayleigh wave travels along the surface $\theta_2 = \theta_R = 90°$, Snell's law yields

$$\theta_D = arcsin\left(\frac{c_D^{wedge}}{c_R^{sample}}\right) \tag{24}$$

This equation is only solvable for $c_D^{wedge} < c_R^{sample}$, therefore the wedge has to be made up of a material with a much slower wave velocity.

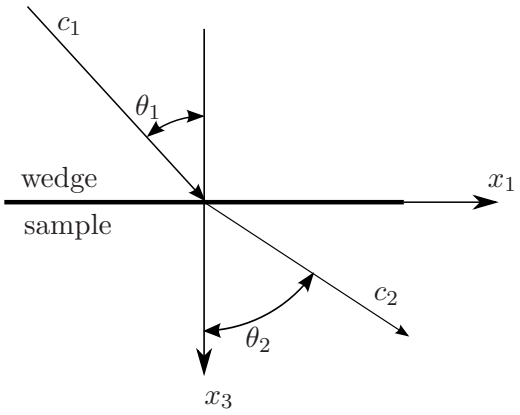

Figure 2.2: Generation of Rayleigh waves

2.3 Rayleigh Waves

Rayleigh surface waves are a special type of acoustic surface waves that travel along a stress-free boundary. They include both longitudinal and transversal motion, and as every surface wave the displacement decays exponentially with depth, i.e., the effect is limited to a shallow layer of approximately one wavelength below the surface.

The characteristic equation of a Rayleigh wave is derived by considering a two dimensional plane wave propagating in x_1-direction with the phase velocity c_R, and the x_3-direction points into the infinite half space, as shown in figure 2.3.

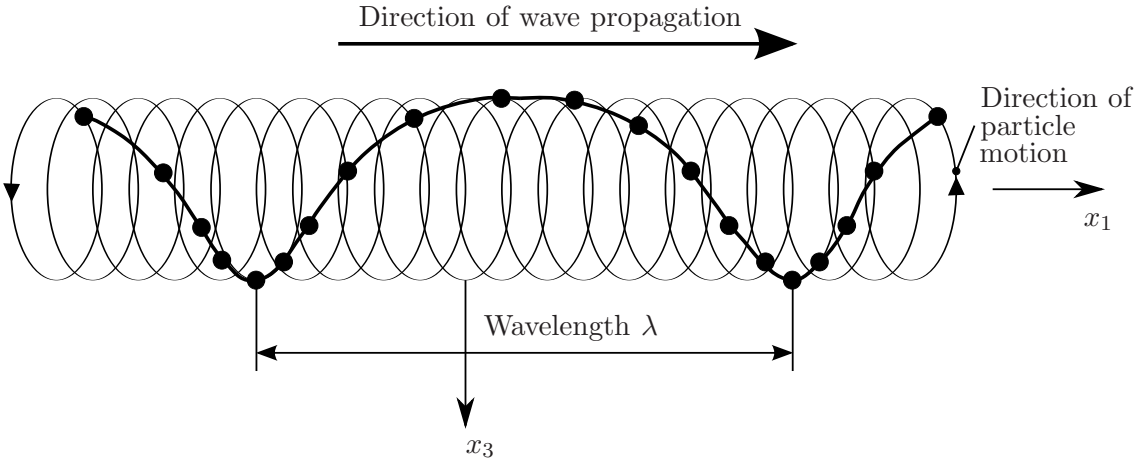

Figure 2.3: Two dimensional motion of a Rayleigh wave in the x_1x_3-plane

The displacement of the Rayleigh wave can also be written as a displacement potential

$$\vec{u} = \nabla\Phi + \nabla \times \vec{\Psi} \tag{25}$$

This potential expression is more general since it considers all possible motions in the half space. The scalar potential Φ and the three components of the vector potential $\vec{\Psi}$ have the form

$$\Phi = Ae^{-\kappa_D x_3} e^{i(k_R x_1 - \omega t)} \tag{26}$$

$$\Psi = Be^{-\kappa_S x_3} e^{i(k_R x_1 - \omega t)} \tag{27}$$

where k_R is the Rayleigh wavenumber and the relationship $c_R = \frac{\omega}{k_R}$ provides the phase velocity of the Rayleigh wave. For increased transparency, we define $\kappa_D = \sqrt{1 - (\frac{c_R}{c_D})^2}$ and $\kappa_S = \sqrt{1 - (\frac{c_R}{c_S})^2}$. As already mentioned, the derivation considers only a two dimensional plane wave that propagates in x_1-direction, therefore the potentials simplify significantly. With $u_2 = 0$:

- $\frac{\partial}{\partial x_2} = 0$
- $\Psi_1 = \Psi_3 = 0$
- and $\Psi_2 = \Psi$

If we apply these conditions and consider that a Rayleigh wave travels along a stress-free surface why the normal τ_{33} and transverse τ_{31} stresses have to be zero at $x_3 = 0$, we obtain the Rayleigh characteristic equation

$$(\kappa_S^2 + k_R^2)^2 - 4\kappa_S \kappa_D k_R^2 = 0 \tag{28}$$

The characteristic equation (28) shows that Rayleigh surface waves are nondispersive since the phase velocity is completely independent of the frequency f. A good approximation of the characteristic equation is given in [1] by

$$c_R \approx \frac{0.862 + 1.14\nu}{1 + \nu} c_S \tag{29}$$

This approximation is fulfilled by all solid materials since it is valid for $0 < \nu < 0.5$. For traditional metallic materials is $\nu = 0.2...0.34$ which implies that the Rayleigh velocity is about 90% of the shear wave velocity. We have shown above that $c_D > c_S$ for any material, so we can conclude that the Rayleigh wave arrives after the shear and longitudinal wave since $c_R < c_S < c_D$.

2.4 Extension to Nonlinear Wave Propagation

So far, we only consider linear wave propagation in materials with an ideally linear stress-strain relationship. However, heterogeneous materials with different phases or materials in a damaged stage do not follow the linear version of Hooke's law. An extension of the linear version of Hooke's law is necessary. If a sinusoidal wave with a certain frequency is introduced into a nonlinear material, the wave is distorted by the nonlinear elastic response of the material and higher harmonics are generated, as depicted in figure 2.4.

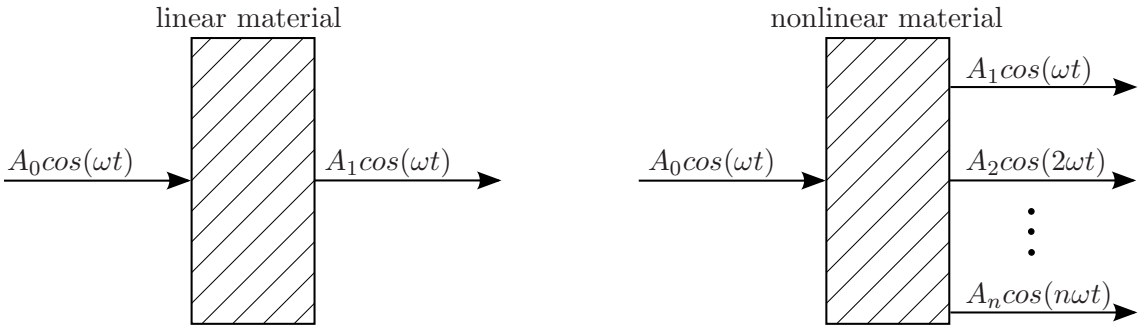

Figure 2.4: Generation of higher harmonics in nonlinear materials

The higher harmonics' amplitudes, especially of the second harmonic, provide information about the nonlinearity of the material. The non-dimensional nonlinearity parameter β, derived in chapter 2.4.1, relates the first and second harmonic and is used as indicator for the stage of thermal aging. The measurable nonlinearity is generated by different causes like precipitations, dislocations, vacancies and microcracks (chapter 4).

2.4.1 Derivation of the Nonlinearity Parameter β

Since the whole derivation of the nonlinearity parameter β would be out of scope of this research, this chapter deals with the main steps of the derivation. However, it is noteworthy to refer on Hamilton and Blackstock [12], where a detailed derivation of the nonlinearity parameter β can be found. It is based on the specific strain energy per unit mass W, which is only dependent on local stretching and volume change.

By combining the equation of motion (1) and the specific strain energy W, we obtain the general nonlinear wave equation

$$\rho\frac{\partial^2 u_i}{\partial t^2} = \frac{\partial^2 u_k}{\partial x_j \partial x_l}\left(C_{ijkl} + M_{ijklmn}\frac{\partial u_m}{\partial x_n}\right) \tag{30}$$

where C_{ijkl} depicts the fourth order stiffness tensor and

$$M_{ijklmn} = C_{ijklmn} + C_{ijln}\delta_{km} + C_{jnkl}\delta_{im} + C_{jlnm}\delta_{ik} \tag{31}$$

the higher order stiffness tensor. Equation (30) can be simplified by considering a one dimensional longitudinal wave, propagating in the x_1-direction and applying Voigt's notation for the second and third order elastic constants ($C_{ijklmn} = C_{IJK}$)

$$\frac{\partial^2 u_1}{\partial t^2} = \frac{1}{\rho}\frac{\partial^2 u_1}{\partial^2 x_1}\left(C_{11} + (C_{111} + 3C_{11})\frac{\partial u_1}{\partial x_1}\right) \tag{32}$$

The elastic constants can be replaced by the second and third-order Huang coefficients A_e and B_e [12], respectively.

$$A_e = C_1 + C_{11} \qquad\qquad B_e = C_{111} + 3C_{11} \tag{33}$$

where C_1 represents the initial stress. Plugging equation (33) into (35), setting the initial stress to zero and using $c_D^2 = \frac{A_e}{\rho}$, we can express the nonlinear equation of motion for the one dimensional case as

$$\frac{\partial^2 u_1}{\partial t^2} = \frac{\partial^2 u_1}{\partial^2 x_1}c_D^2\left(1 + \frac{B_e}{A_e}\frac{\partial u_1}{\partial x_1}\right) \tag{34}$$

The nonlinearity parameter can be attained by

$$\frac{\partial^2 u_1}{\partial t^2} = \frac{\partial^2 u_1}{\partial^2 x_1}c_D^2\left(1 - \beta\frac{\partial u_1}{\partial x_1}\right) \qquad for \qquad \beta = -\frac{B_e}{A_e} \tag{35}$$

Moreover, the one dimensional wave equation can be set up in terms of a second order elastic constant P and Q, where the latter is a combination of second and third order elastic constants. This description is used in section 4.4 to derive the contribution of dislocations in the lattice.

$$\frac{\partial^2 u_1}{\partial t^2} = \frac{\partial^2 u_1}{\partial^2 x_1}c_D^2\left(P + Q\frac{\partial u_1}{\partial x_1}\right) \tag{36}$$

where, consequently

$$\beta = -\frac{Q}{P} \tag{37}$$

yields the nonlinearity parameter.

To solve equation (35), we apply the perturbation theory. This theory can be used if we assume that the displacement u composes as follows

$$u = u_0 + u' \tag{38}$$

with u_0 as the displacement of the initially excited wave and u' represents the first order perturbation solution. If we take a harmonic excitation of the form $u_0 = A_1 cos(k_D x - \omega t)$, $k_D = \frac{\omega}{c_D}$ and apply this theory, it leads to the displacement

$$u = A_1 cos(k_D x - \omega t) - A_2 sin2(k_D x - \omega t) \tag{39}$$

which can be solved as

$$u = u_0 cos(k_D x - \omega t) - \frac{\beta}{8} k^2 u_0^2 x sin2(k_D x - \omega t) \tag{40}$$

By comparing the coefficients of equation (39) and (40) the nonlinearity parameter equals

$$\beta = \frac{8A_1^2}{A_2 k_D^2 x} \tag{41}$$

The nonlinearity parameter β depends on the amplitude of the fundamental and second harmonic wave (A_1 and A_2), the longitudinal wavenumber k_D and the propagation distance x. Thus, it is easy to determine β since the amplitudes A_1 and A_2 can be experimentally identified by using a certain wavenumber k_D and propagation distance x.

2.4.2 Nonlinearity Parameter β for Rayleigh Waves

The nonlinearity parameter β is only valid for longitudinal waves; however, a Rayleigh wave propagates in a two dimensional space which complicates the derivation. While a longitudinal wave is sensitive with respect to the generation of higher harmonics, the nonlinearity of a shear wave vanishes in isotropic materials due to the symmetry of the third order coefficient B_e. But as we consider that Rayleigh waves are the superposition of a longitudinal and shear wave, a Rayleigh wave should behave in a similar way as the longitudinal wave. Therefore, β also depends on the ratio of A_2 and A_1^2.

The following derivation for the nonlinear Rayleigh wave is based on Hermann et al. [13], Hikata et al. [14] and Viktorov [25]. As described in section 2.3, we consider a Rayleigh wave

propagating in x_1-direction and the x_3-axis points into the half space. According to [25], the displacement potentials we use in (26) and (27) can be rewritten as

$$\Phi = -i\frac{A_1}{k_R}e^{-\kappa_D x_3}e^{i(k_R x_1-\omega t)} \tag{42}$$

$$\Psi = -i\frac{B_1}{k_R}e^{-\kappa_S x_3}e^{i(k_R x_1-\omega t)} \tag{43}$$

If we apply the same boundary condition of a stress-free surface the constants A_1 and B_1 are related as follows

$$A_1 = -i\frac{2k_R\kappa_D}{k_R^2+\kappa_S^2}B_1 \tag{44}$$

Recalling the fact that a Rayleigh wave is the superposition of a longitudinal and shear wave with the same trace velocity, the displacement can be decomposed into a longitudinal (here x_1) and shear (here x_3) part and with the substitution of B_1 with A_1 (44)

$$u_{x1}(\omega) = A_1\left(e^{-\kappa_D x_3} - \frac{2\kappa_D\kappa_S}{k_R^2+\kappa_S^2}e^{-\kappa_S x_3}\right)e^{i(k_R x_1-\omega t)} \tag{45}$$

$$u_{x3}(\omega) = iA_1\frac{\kappa_D}{k_R}\left(e^{-\kappa_D x_3} - \frac{2k_R^2}{k_R^2+\kappa_S^2}e^{-\kappa_S x_3}\right)e^{i(k_R x_1-\omega t)} \tag{46}$$

According to Zabolotskaya [30], the second order harmonic in a material with a weak quadratic nonlinearity is approximately given by

$$u_{x_1}(2\omega) \approx A_2\left(e^{-2\kappa_D x_3} - \frac{2\kappa_D\kappa_S}{k_R^2+\kappa_S^2}e^{-2\kappa_S x_3}\right)e^{i2(k_R x_1-\omega t)} \tag{47}$$

$$u_{x_3}(2\omega) \approx iA_2\frac{\kappa_D}{k_R}\left(e^{-2\kappa_D x_3} - \frac{2k_R^2}{k_R^2+\kappa_S^2}e^{-2\kappa_S x_3}\right)e^{i2(k_R x_1-\omega t)} \tag{48}$$

Since the shear wave contribution does not lead to the generation of higher harmonics, it is permitted to relate the amplitudes of the fundamental and second harmonic by using the nonlinearity parameter β. As for the longitudinal bulk wave, we obtain β that is dependent on A_1, A_2, wavenumber k_D and propagation distance x (here x_1).

In this research an air-coupled transducer is used to detect the wave. The air-coupled transducer only measures the out-of-plane motion of the Rayleigh wave, so we have to relate the particle displacement u_{x3} on the surface of the infinite half space to β. From equation (46) and (48), the ratio of the second harmonic to the fundamental amplitude is

$$\frac{u_{x_3}(2\omega)\mid_{x3=0}}{u_{x_3}(\omega)\mid_{x3=0}} = \frac{\beta k_D^2 x}{8i\frac{\kappa_D}{k_R}\left(1-\frac{2k_R^2}{k_R^2+\kappa_S}\right)} \tag{49}$$

The nonlinearity parameter β is related to the out-of-plane displacement by

$$\beta = \frac{u_{x_3}(2\omega)\mid_{x3=0}}{u_{x_3}(\omega)\mid_{x3=0}} \frac{8i\kappa_D}{xk_D^2 k_R}\left(1 - \frac{2k_R^2}{k_R^2 + \kappa_S}\right) \tag{50}$$

It has to be mentioned that the shear wave component does not produce nonlinearity by itself. However, the second term in the brackets of equation (50) contains the contribution of the shear wave component (i.e. κ_S) that interacts with the longitudinal one.

CHAPTER III

PREPARATION AND MICROSCOPIC STRUCTURE OF MODIFIED 9%CR FERRITIC MARTENSITIC STEEL

As mentioned above, 9-12%Cr ferritic martensitic steels have attracted significant attention, due to their high temperature performance (up to 650°C and higher) [20]. 9-12%Cr steels comply with the basic requirements of creep strength and oxidation resistance at a low cost. Another well-known material, that satisfies these requirements, is austenitic stainless steel; however, this steel is relatively expensive and thus from an economic point of view not applicable. Furthermore, it contains a poor thermal cycling capability, so it is unsuitable for thick-section components like piping, large forgings and castings of steam power plants.

Beginning with the 12CrMoV steel X20, introduced in the mid-1950s, alloy developments over the last decades have led to a steady increase in performance like the modified P91 (1970s) and P92 (1980s) [7]. Improved creep resistance is achieved by small but important changes in composition. These changes include additional small amounts of elements like vanadium (V), niobium (Nb), nitrogen (N), tungsten (W) or molybdenum (Mb). Historically, isothermal tests with metallurgically stable material are expected to have a linear relation between the logarithm of time and the logarithm of stress. However, their initially evaluation of long-term thermal aging or creep strength at about 600°C are not reliable and a gradual decrease in mechanical properties at temperatures above 593°C are reported in Jablonski et al. [16]. The unexpected over-estimation of long-term properties is a consequence of evolutions in the microstructure during operating temperature. The major microstructural changes, namely the precipitates, are described in detail in section 4.3.

This research concerns the modified 9%Cr ferritic martensitic steel and begins with the description of the production and geometry of the samples provided.

3.1 Preparation of 9%Cr Steel

The specimens are normalized and tempered according to [8].

Table 3.1: Preparation of specimen

	Temperature [°C]	Time [min/mm]	Cooling method
Normalizing	1050	1	still air
Tempering	770	3	still air

Normalizing has to be around 1050°C since it has to be inside the austenitic loop [7] to obtain an exclusive austenitic microstructure. After cooling at still air to room temperature, the steel should become fully martensitic with a high dislocation density. As the normalized steel is hard and brittle, it has to be tempered at 770°C to recover ductility of the steel. The minimum chromium content of about 9% is determined by the oxidation resistance at operation temperature, and the maximum content is restricted to about 12% in order to stay in the austenitic loop. If we leave the austenitic loop and ferrite is present during normalizing, the steel does not completely transform to martensite. This section indicates a rough overview on the production, further details on this topic can be found in [7] and [16].

3.2 9%Cr Steel Composition and Mechanical Properties

The composition of 9%Cr steel comprises at least the following elements: chromium (Cr), molybdenum (Mo), carbon (Cr), titanium (Ti) and other elements with the balance iron (Fe). Table 3.2 breaks down the chemical composition of the provided specimens.

Table 3.2: Composition of modified 9%Cr steel

Element	C	Mn	P	S	Si	Cu	Ni	Cr	Mo
Percentage(%)	0.117	0.443	0.020	0.0005	0.330	0.090	0.153	8.888	0.862

Element	Al	Nb	V	Ti	N
Percentage(%)	0.011	0.073	0.192	0.003	0.0451

In the following, we aim to present some elements to understand the importance of the alloy and the later precipitations described in section 4.3.

As can seen from table 3.2, chromium (Cr) is the main alloying element since it gives a satisfying level of hot corrosion resistance, and it is essential to ensure high temperature oxidation resistance. This alloy does not only indicate the name of the steel, its considerable amount enables the high temperature performance.

Molybdenum (Mo) is the second important alloy to achieve the desired properties. A content of at least 0.5% Mo is needed for solution strengthening and improves the creep strength. However, during service conditions in high temperature, Mo creates an intermetallic phase, the so called Laves phase (section 4.3), that significantly impacts the toughness and, moreover, its presence reduces the time of operation.

Titanium (Ti) provides the same properties as chromium, it improves the creep strength and oxidation resistance. Specifically for this alloy element is the formation of large primary and small secondary precipitates with carbon (C). The primary precipitates are responsible for grain boundary pinning, whereas the secondary should impede the glide and climb of dislocations throughout the microstructure.

Niobium (Nb) and vanadium (V) combine with carbon (C) and nitrogen (N) to form a finely dispersed precipitation of the form (Nb,V)(C,N), which has a beneficial effect for improving the long-term performance.

Table 3.3 provides results of mechanical tests, conducted at room temperature (20°C) by [8].

Table 3.3: Mechanical properties of modified 9%Cr steel

Yield strength $R_{0.2\%}$	620	MPa
Tensile strength R_m	755	MPa
Elongation A_{50}	26	%
Vickers hardness	235	$HV10$

3.3 Geometry of Specimens

Figure 3.1 shows the geometry of the specimens. The dimension gauge of the rectangular specimen is $8inches$ x $1.8inches$ x $0.5inches$ in length, width, and height, respectively.

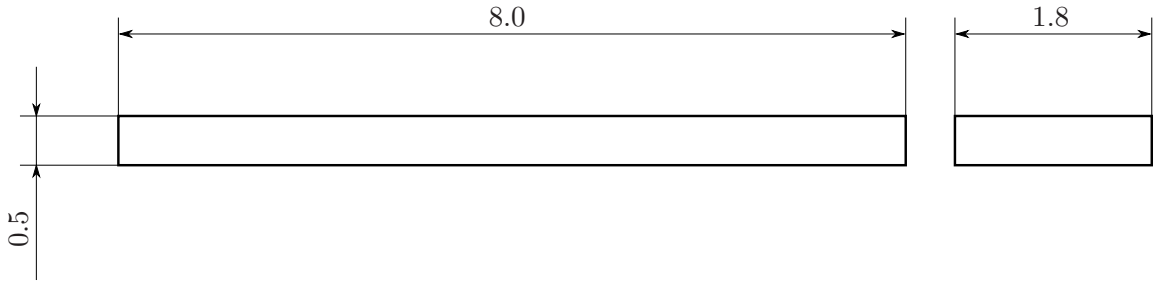

Figure 3.1: Drawing of the undamaged sample, all dimensions in inches

It has to be noted that the width and height must be chosen in such a way that the Rayleigh wave can propagate unimpeded. The minimum height is determined by the relationship of the phase velocity c_R, frequency f and wave length $\lambda = \frac{c_R}{f}$. If we conservatively take a phase velocity of $3000\frac{m}{s}$ and an exciting frequency of $2.1MHz$, we obtain a wavelength of around $1.43mm$. This is equivalent to $0.0625inches$, so the height is much larger than the wave length (height $>> \lambda$). Since the Rayleigh wave only penetrates one time of its wavelength into the material, no reflection from the back side (bottom) of the specimen is expected.

The second geometric restriction is determined by the width of the wedge ($1inch$) and the active diameter of the exciting transducer ($0.5inches$). If we very conservatively assume that the beam of the transducer spreads over the whole width of the wedge, then the width of the specimen should be at least $1inch$. Since we have a width of $1.8inches$, it can be said, with a measure of certainty, that the edges do not influence the wave. Consequently, the conservatively dimensioned specimen allows an unimpeded propagation of Rayleigh waves and ensures that no interference will occur.

CHAPTER IV

MICROSTRUCTURAL CHANGES DUE TO THERMAL AGING

During thermal aging certain alloy steels form precipitations that improve the hardness. The initially supersaturated element produces finely distributed precipitations of an impurity phase, which impede the free sliding motion of dislocations. The hardening effect is based on the introduced obstacles (precipitates) that hinder the movement of dislocations and increase the yield stress.

Besides precipitation hardening, solid solution strengthening of molybdenum has been associated with the creep strength of 9%Cr steels. According to [11], it can be expected that solid solution strengthening does not significantly affect long-term microstructural stability. Further information to support this assumption can be found in section 4.3.2. So, precipitation hardening by pinning of dislocations and sub-grain boundaries is the most significant strengthening mechanism. However, as mentioned in [5], [11] and [20] unexpected drops in the mechanical properties appear, and since 9%Cr steels mainly rely on precipitates for their high temperature performance, it is of major importance to understand the process.

Therefore, section 4.2 and 4.3 give a detailed description of the mechanisms that have an impact on the nonlinearity parameter β. Section 4.4 describes the correlation between the microstructural properties and the nonlinearity parameter. In other words, the change in the microstructure can be related to the nonlinearity parameter β. Consequently, any change in the nonlinearity may allow for an early assessment of the stage of thermal aging.

4.1 Thermal Aging and Preparation for Testing

The samples are received from the manufacturer and we choose a heat treatment schedule (table 4.1) to obtain several precipitation stages. Every sample undergoes an isothermal heat treatment at 650°C for $200h, 500h, 1000h, 1500h$ or $3000h$, respectively. We use a small interval between exposure times in the beginning since we want to investigate the early stages of the thermal aging.

Table 4.1: Heat treatment of specimen

Sample #	Temperature [°C]	Time [h]
Sample 1	650	0
Sample 2	650	200
Sample 3	650	500
Sample 4	650	1000
Sample 5	650	1500
Sample 6	650	3000

As can seen in table 4.1, sample 1 has a treatment time of $0h$ and it shall serve as an untreated reference specimen. After the heat treatment schedule is conducted, the surface is hand polished in order to remove all debris and visible texture effects from the production and heat treatment, which may influence the ultrasonic measurements. To receive comparable results, it is important to ensure the same surface quality.

4.2 Mechanisms During Thermal Aging of Modified 9%Cr Steel

The precipitation process can be subdivided in three stages; it starts with the nucleation, followed, if the nuclei reaches a certain size, by the growth, and finally coarsening. Generally speaking, the hardening mechanism is based on finely distributed precipitates interacting with sub-grain boundaries or dislocations. This mechanism is very complicated and there is a huge interaction during thermal aging. However, contribution of precipitated particles to creep strength have similarities to the Orowan stress [7]; thus, the relationship can be estimated by the Orowan stress. The following equation shows the relationship between Orowan stress and the precipitate volume fraction f_p, and radius of precipitated particles r_p:

$$\sigma_{Orowan} = 3.32\frac{G|\vec{b}|\sqrt{f_p}}{2r_p} \tag{51}$$

where G is the shear modulus and $\vec{b}$ represents the Burgers vector. For this research the derivation of this equation is not as important as its interpretation. Equation (51) predicts that larger volume fraction and smaller precipitates enhance the Orowan stress and thus the creep strength.

4.2.1 Nucleation, Growth and Coarsening

Nucleation can be divided in a homogeneous and heterogeneous process. The former appears spontaneously and randomly without a preferred nucleation site, whereas for the latter defects in the crystal structure, like dislocations, grain boundaries or other precipitates, serve as starting point. Since the specimen has many dislocations, the heterogeneous nucleation is dominant. The process is mainly driven by thermodynamic forces and interfacial energy, but the amount of the necessary element also affects the process. Therefore, we can modify the precipitation by adjusting the composition. By controlling the precipitates, we are able to benefit the creep strength because an increase in the amount of certain elements can lead to a fast nucleation rate, many small particles form and strengthen the long-term properties. If the rate is slow, the early nucleated precipitates have time to grow. This results in very few big particles that have a negative impact (see equation (51)) on creep resistance.

As soon as the nuclei reaches a certain size, the growth phase begins. The growth continues until the precipitates have the same chemical potential as the dissolved elements in the matrix. In this phase the volume fraction f_p and precipitate size r_p grow influencing the nonlinearity parameter β (section 4.4). The growth is primarily diffusion controlled and highly depending on the type of particles. More information are given in section 4.3 and [11].

The last stage of precipitates is coarsening, also called Ostwald ripening [7]. This stage can be characterized by the further growth of the largest particles by the expense of the smaller ones. Since no new particles are formed, the number of particles declines but the volume fraction f_p remains the same. Obviously, this process impacts negatively the Orowan stress since the finely distributed precipitates are replaced by coarse precipitates.

4.2.2 Dislocations and Their Interaction with Precipitations

Dislocations are line defects in a crystal lattice that reduce the amount of free energy in the system. Consequently, parts with a high amount of dislocations are relatively unstable. A very detailed examination of dislocations and precipitation hardening is given in [10], [15] and [18]; in this chapter only some selected information of the study may be mentioned. The goal is to describe how dislocations and precipitates influence each other and the creep strength.

Physically, the strengthening effect depends on the nature of the obstacles, like its size, coherency, crystal structure and chemical characteristics. In the early stages, the strength increases due to nucleation of many small precipitates, that operate as obstacles for dislocation motion, as previously described. The dislocation passes the obstacle by cutting, which results in a resisting force. The resisting force behaves proportional to the size, so as the particle grows, cutting through it becomes more difficult and for a certain radius r_{bow} the obstacle is strong enough to withstand the dislocation, as depicted in figure 4.1a. If $r_p > r_{bow}$ the shear strength and radius are reciprocal. The bowing radius is between approximately $5nm$ and $30nm$. Since the evolving particles during thermal aging have a size of $r_p > 50nm$ the dominant strengthening effect is due to the bowing mechanism.

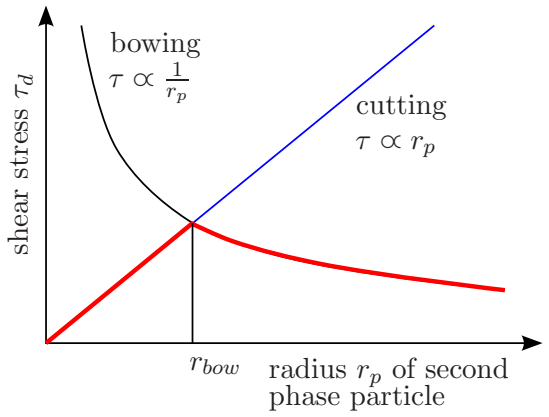

(a) Shear stress τ_d over radius r_p of second phase particles

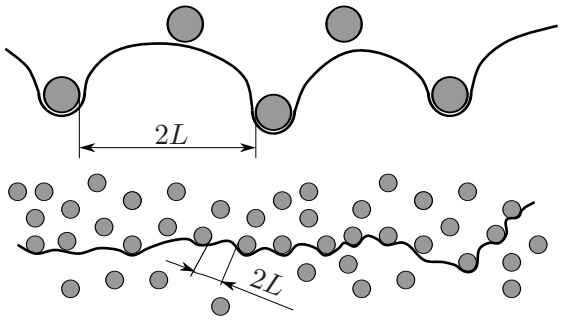

(b) Strong and weak obstacles distributed in a unit area

Figure 4.1: Strengthening effect of dislocations and obstacles

Figure 4.2(a) and (b) show the two bypass mechanisms for absolutely strong and less strong obstacles, respectively. The Orowan mechanism (a) starts with a bowed dislocation between two particles. If the dislocation yields after it becomes semi-circular in shape, an Orowan loop around the particle is formed. This loop makes the motion more and more difficult. Whereas, if yielding occurs before the dislocation becomes semi-circular in shape (b), the dislocation only bows and passes the particle without forming a loop.

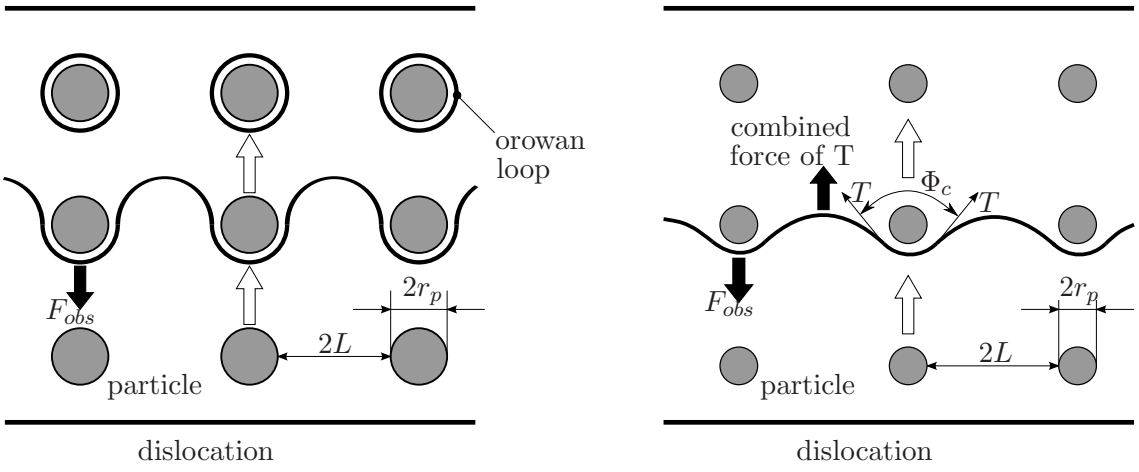

(a) Orowan mechanism (strong obstacles)

(b) Bowed dislocation (less strong obstacles)

Figure 4.2: Bypass mechanisms of dislocations for strong and less strong obstacles

The critical angle Φ_c for the dislocation to overcome the obstacle, the maximum resisting force of an obstacle F_{obs} and the distance $2L$ determine the necessary shear stress τ_d that leads to the hardening effect.

$$F_{obs} = 2L\vec{b}\tau_d \tag{52}$$

Furthermore, we can define the force as

$$F_{obs} = 2Tcos\left(\frac{\Phi_c}{2}\right) \tag{53}$$

With equation (52) and (53), we can say that

$$\tau_d = \frac{Tcos\left(\frac{\Phi_c}{2}\right)}{\vec{b}L} \tag{54}$$

where $\Phi_c \approx 0$ holds for a strong obstacle and $\Phi_c \approx \pi$ for a weak.

It seems that the hardening effect of strong obstacles is more effective because of the term $cos\left(\frac{\Phi_c}{2}\right) \approx 1$ compared to weak obstacles with $cos\left(\frac{\Phi_c}{2}\right) \approx 0$. However, weak obstacles are generally much smaller than strong obstacles. This implies that more weak obstacles are distributed in a unit area, and therefore $2L$ is much smaller, as illustrated in figure 4.1(b) So, even though F_{obs} is small, the shear stress τ_d can be large. This mathematical approach is used in section 4.4 to derive the contribution of dislocations on the nonlinearity parameter β.

Furthermore, not only the size of precipitates changes over aging time, but also the dislocation density decreases while tempering and aging, [20] and [21]. According to results of Sawada [21] with a similar material, the initial density after normalizing of $19 \cdot 10^{14} m^{-2}$ steadily diminishes to $6.1 \cdot 10^{14} m^{-2}$ after tempering and $1.6 \cdot 10^{14} m^{-2}$ after aging. Creep deformation even accelerates the decrease in dislocation density. Moreover, Park et al. [20] shows that the lath martensite, containing a high dislocation density, dissolves into sub-grain after thermally aged. Consequently, the density quickly declines in the beginning since more martensite is transformed, and reaches a certain equilibrium state, as qualitatively illustrated in figure 4.3. Furthermore, the aging temperature affects the decline and the equilibrium state of the dislocation density. For higher temperature, the slope at the beginning is higher and the density reaches a lower equilibrium state. Park et al. [20] showed that an increase from 593°C to 700°C reduces the density after $5000h$ from $7 \cdot 10^9 cm^{-2}$ to $4.5 \cdot 10^9 cm^{-2}$ starting at $10 \cdot 10^9 cm^{-2}$.

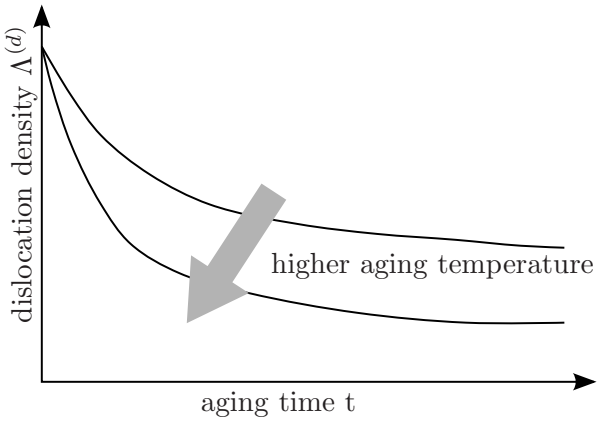

Figure 4.3: Dislocation density $\Lambda^{(d)}$ over aging time

4.3 Precipitates in Modified 9%Cr Steel

This section considers only the precipitates most frequently appearing and probably having influence on the nonlinearity parameter β. The link between precipitates and β is established in section 4.4. Table 4.2 divides the evolving precipitated particles into two classes. At the top are the precipitates that evolve during tempering and at the bottom during thermal aging.

Table 4.2: Most common precipitates in 9%Cr steels

Precipitate	Chemical Formula	Comments
$M_{23}C_6$	$(Cr, Fe, Mo)_{23}C_6$	Precipitates during tempering most stable carbide
MX	$(Nb, V)(N, C)$	Undissolved during austenization
M_2X	Cr_2N	Precipitates during tempering thermodynamically stable
Lave Phase	$(Fe, Cr)_2Mo$	Precipitates during creep exposure or thermal aging ($T < 700°C$)
Z-Phase	$Cr(Nb, V)N$	Precipitates during creep exposure or thermal aging but for longer holding times

There are other precipitates that will not be mentioned in this research but can be found in [7]. Especially, the Laves phase and Z-phase are interesting since no one has perfectly been aware of the destructive effects or even knowing whether these precipitates are detrimental. Many researches are concerned with the issue of these two phases, like [20] and [29] with Laves phase and [6], [7] and [23] with Z-phase. Figure 4.4 illustrates exemplary the most common precipitates mentioned above in table 4.2, with the Laves and Z-phase highlighted by a red box.

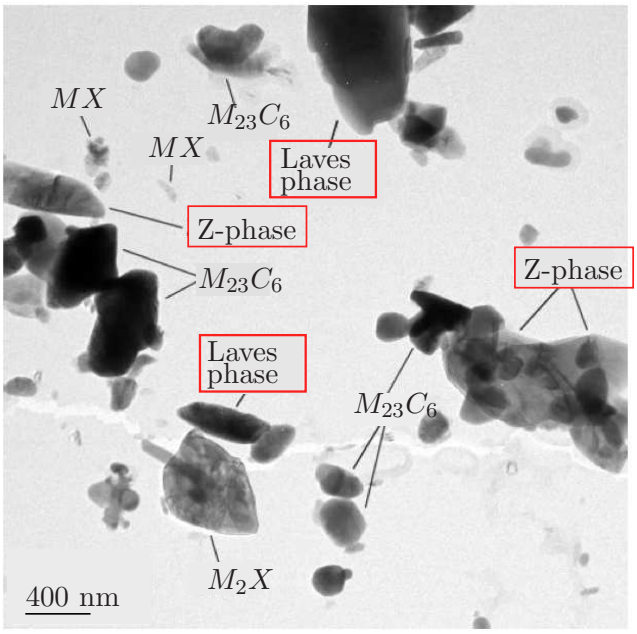

Figure 4.4: Exemplary illustration of the precipitates in 9%Cr steels [7]

4.3.1 $M_{23}C_6$, MX and M_2X

All these phases form during the tempering process and they are thermodynamically stable. Cipolla [5] and Hald [11] conduct heat treatments with similar materials (amount of some composition varies) to determine the microstructural evolution during thermal aging. The following graphs and values are derived from their results.

$M_{23}C_6$ represents the most stable carbide after tempering. In general, it is the most abundant precipitation after tempering. The nucleation mainly occurs on prior austenite grain boundaries and martensite lath boundaries. At the beginning of the thermal aging, the average radius of the carbides is about $100nm$ with a relatively high coarsening rate but even after $10000h$ at temperature 650°C is the critical radius of $250nm$ not reached [5], as depicted in figure 4.5 (green broken line).

The nitrogen content determines the stability of M_2X precipitates but even with a low nitrogen it is relatively stable. It tends to occur with lower tempering temperatures by substituting MX precipitates. However, M_2X is rarely desired since it usually gets large and decreases creep strength.

The last particles, precipitating before thermal aging, have the form MX. They primarily form in V and Nb rich areas combining with N or C, respectively. We can subdivide these precipitates into two groups; austenization produces the primary MX and the secondary MX evolves during tempering. However, additional information can be obtained in [7]. Both types are very stable against coarsening, as illustrated in figure 4.5 (blue dotted line), and can be seen as the backbone of the long-term stability.

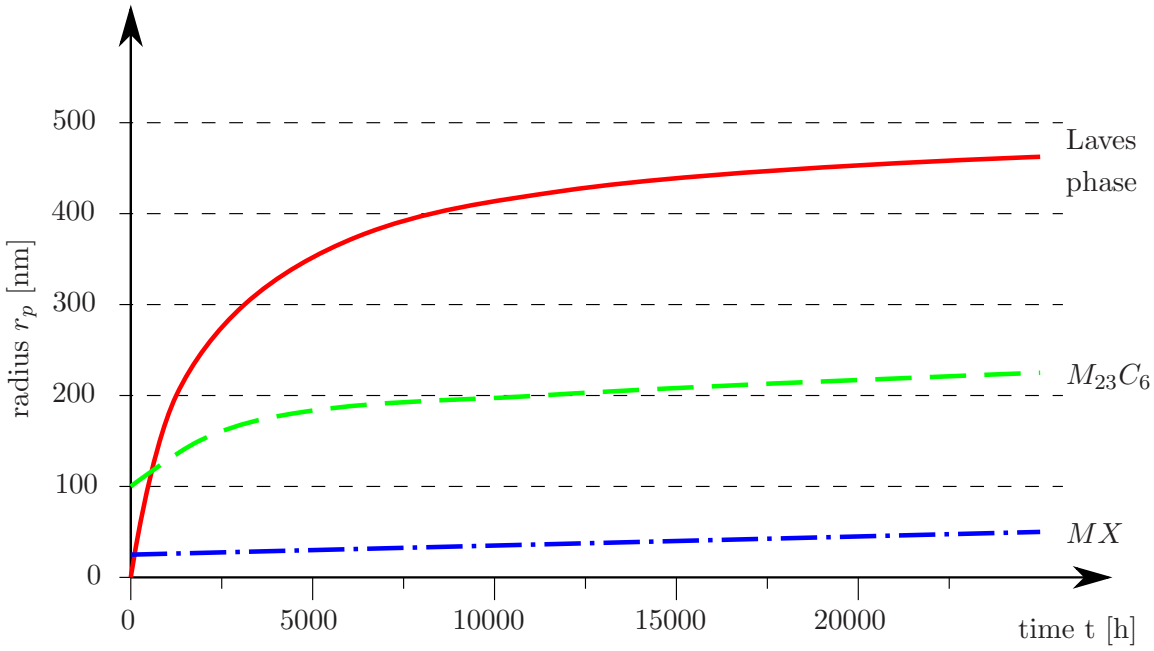

Figure 4.5: Microstructural size evolution of $M_{23}C_6$, MX and Lave phase in 9%Cr steels

4.3.2 Laves Phase

Laves phase results due to Mo containing in the steel. It is an intermetallic phase having the general composition A_2B and a hexagonal crystal structure. In particular, the two linking atoms have to have a size ratio of about $\sqrt{\frac{3}{2}} \approx 1.225$ to form Laves phase. This explains why a molybdenum atom ($2.01\mathring{A}$) tends to create an intermetallic phase with iron atoms ($1.72\mathring{A}$).

$$ratio_{Lave} = \frac{r_{Mo}}{r_{Fe}} = \frac{2.01\mathring{A}}{1.72\mathring{A}} \approx 1.17 \tag{55}$$

Laves phase may also contain little amounts of Cr and Si. It is very unstable at high temperature (above 700°C) [5], therefore it does not nucleate during tempering as the other

precipitates. It forms during thermal aging and rapidly grows up to a size of about $400nm$ the first $1000-10000h$, as depicted in figure 4.5 (red solid line), and it has a long nucleation and growth phase [11]. From the creep strengthening point of view, Laves phase has two aspects. On the one hand, high amounts of Mo are transformed into an intermetallic phase, resulting in a creep instability due to the loss of the solid solution strengthening effect from Mo. This opinion was supported by the breakdown of creep strength of several 9%Cr steels [11]. However, good long-term results of the 9%Cr steel P92 contradicts the opinion. Furthermore, the actual contribution of the solid solution strengthening mechanism is sparse since the experimental proof to demonstrate and quantify its effect is difficult. This contradiction is consistent with improved creep strength by compositional changes resulting in changes of the precipitation populations.

On the other hand, the increased volume fraction at the beginning of the precipitation phase enhances the creep strength since Laves phase is a finely dispersed phase (see Orowan equation (51)). However, as mentioned above, the growth rate is comparatively high, so the radius of the particles reaches quickly very large sizes with a detrimental effect.

4.3.3 Z-Phase

The Z-phase is the most stable nitride in 9%Cr steel but it only forms after exposure for several thousand hours at $600-650°C$ [7]. Historically, the Z-phase is very interesting since its perception has varied greatly, from beneficial to insignificant to detrimental, and it is still debated. Very little is known about the behavior; however, recent researches are dealing intensively with the impact on long-term properties and partly claim that MX particles may be replaced by the more stable Z-phase, which precipitates as coarse particles and weakens the creep strength. Danielsen [7] provides a detailed consideration of the original and the modified Z-phase and its impact on 9-12%Cr steels. This research does not go into further detail since these precipitates appear only after several thousand hours of exposure. Moreover, the Z-phase is barely observed in steels with a chromium content below 9% [11]. Therefore, we assume that the Z-phase does not precipitate with a maximum thermal aging time of $3000h$ and a chromium content of 8.888%.

4.4 Impact of Dislocations and Precipitations on Nonlinearity

So far, we examine the microstructure of the material in detail and consider all relevant mechanisms during thermal aging. This section provides the theoretical background that enables the assessment of the stage of thermal aging. Based on the derived nonlinearity parameter β in section 2.4.2, we can use the fundamental achievements of Hikata et al. [14], who investigated the impact of pinned dislocations, and the further studies on the relationship between nonlinearity parameter and volume fraction f_p and radius of the precipitates r_p by Cantrell et al. [4].

4.4.1 Mathematical Derivation of the Contribution of Dislocations and Precipitates on β

We can derive the relation between applied stress and displacement of dislocations, by considering a small longitudinal stress σ having a resolved shear stress component $\tau_d = R\sigma$ in the slip plane. R represents the conversion factor that enables the calculation of a shear stress τ_d based on an applied longitudinal stress σ.

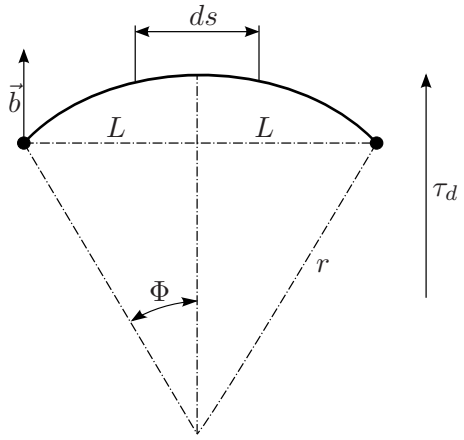

Figure 4.6: Bowed out dislocation undergoing shear stress

If the dislocation is pinned at two points with the distance $2L$, it is bowed out by a shear stress τ_d and forms a dislocation line to be in an arc shape with radius r and angle 2Φ, as depicted in figure 4.6. If we assume that the dislocation density is small enough that the interaction among them can be neglected, the shear stress can be expressed by

$$\tau_d = \frac{\mu|\vec{b}|}{2r} \tag{56}$$

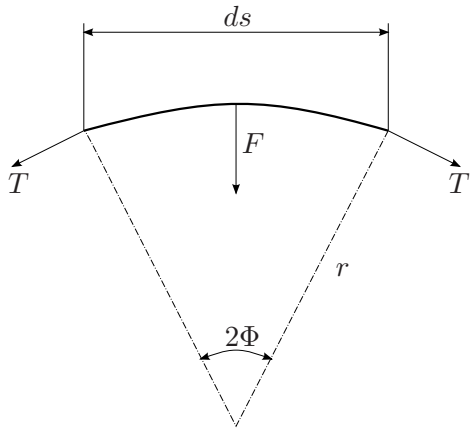

Figure 4.7: Infinitesimal dislocation line under line tension T

Considering an infinitesimal line segment with the length ds, the line tension acts on both sides, as illustrated in figure 4.7. That results in a projected force F, showing towards the center of the arc. The force can be written as $F = 2Tsin(\Phi)$ and the angle Φ can be related to the line segment ds and radius r by $sin(\Phi) = \frac{ds/2}{r}$. Combining these two equations, it leads to

$$F = \frac{Tds}{r} \tag{57}$$

Assuming the dislocation is approximately bowed by the same order of the length of the Burger's vector, we can define the force as $F = \tau_d|\vec{b}|ds$. Subsequently, we substitute the force F with equation (56) and (57)

$$T = \frac{1}{2}\mu|\vec{b}|^2 \tag{58}$$

where the line tension T is independent of the radius of curvature r. Generally speaking, the shear strain γ_d in a dislocation network can be written as follows

$$\gamma_d = \frac{\Lambda^{(d)}|\vec{b}|}{2L}S_d \tag{59}$$

where $\Lambda^{(d)}$ stands for the dislocation density and S_d denotes the area swept out by each dislocation loop, which can be calculated by

$$S_d = r^2\left(\Phi - \frac{1}{2}sin(2\Phi)\right) \tag{60}$$

Using equation (56), (60) and substituting in equation (59), we obtain the shear strain in terms of a longitudinal stress σ

$$\gamma_d = \frac{2}{3}\frac{\Lambda^{(d)}L^2R}{\mu}\sigma + \frac{4}{5}\frac{\Lambda^{(d)}L^4R^3}{\mu^3|\vec{b}|^2}\sigma^3 \tag{61}$$

where the first, third and fifth powers in the series expansion of $sin(\frac{L}{r})$ are neglected. Since we apply a longitudinal stress σ, the material undergoes an elastic strain ϵ_e that provides the total stress ϵ by combining with the strain contributed by bowed dislocations ϵ_d.

$$\epsilon = \epsilon_e + \epsilon_d \tag{62}$$

If we use the same approach as in section 2.4.1, we obtain the longitudinal stress σ in terms of ϵ_e and the second and third order Huang coefficient.

$$\sigma = A_e\epsilon_e + \frac{1}{2}B_e\epsilon_e^2 \tag{63}$$

or rearrange to solve for ϵ_e

$$\epsilon_e = \frac{1}{A_e}\sigma - \frac{1}{2}\frac{B_e}{A_e^3}\sigma^2 \tag{64}$$

The total strain ϵ can be expressed by plugging equation (61) and (64) into (62) and using the conversion factor Ω introduced by Hikata et al. [14]. The factor has the same purpose as R, it converts the shear strain γ_d into ϵ_d.

$$\epsilon = \left(\frac{1}{A_e} + \frac{2}{3}\frac{\Lambda^{(d)}L^2R\Omega}{\mu}\right)\sigma - \frac{1}{2}\frac{B_e}{A_e^3}\sigma^2 + \frac{4}{5}\frac{\Lambda^{(d)}L^4R^3\Omega}{\mu^3|\vec{b}|^2}\sigma^3 \tag{65}$$

The inverse relation of equation (65) is based on Cantrell [3], who derives ϵ_d by applying a stress perturbation. Hikata et al. [14] examine a Taylor series expansion centered at an initial stress σ_0 resulting in an initial strain ϵ_0. The infinitesimal perturbation $\Delta\sigma$ causing a difference in the strain $\Delta\epsilon$. The stress $\sigma = \sigma_0 + \Delta\sigma$ can be expressed as follows

$$\sigma = \sigma_0 + \left(\frac{\partial\sigma}{\partial\epsilon}\right)\Delta\epsilon + \frac{1}{2}\left(\frac{\partial^2\sigma}{\partial\epsilon^2}\right)\Delta\epsilon^2 \tag{66}$$

or the inversed version according to Cantrell [3]

$$\sigma = \sigma_0 + \left(\frac{\partial\epsilon}{\partial\sigma}\right)^{-1}\Delta\epsilon - \frac{1}{2}\left[\left(\frac{\partial^2\epsilon}{\partial\sigma^2}\right)\left(\frac{\partial\epsilon}{\partial\sigma}\right)^{-3}\right]\Delta\epsilon^2 \tag{67}$$

where the perturbation can be written as

$$\Delta\sigma = \left(\frac{\partial\epsilon}{\partial\sigma}\right)^{-1}\Delta\epsilon - \frac{1}{2}\left[\left(\frac{\partial^2\epsilon}{\partial\sigma^2}\right)\left(\frac{\partial\epsilon}{\partial\sigma}\right)^{-3}\right]\Delta\epsilon^2 = P\Delta\epsilon + \frac{1}{2}Q\Delta\epsilon^2 \tag{68}$$

If we take the partial derivative of ϵ with respect to σ of equation (65), we obtain

$$P = \left(\frac{\partial\epsilon}{\partial\sigma}\right)^{-1} = \left(\frac{1}{A_e} + \frac{2}{3}\frac{\Lambda^{(d)}L^2R\Omega}{\mu} - \frac{B_e}{A_e^3}\sigma + \frac{12}{5}\frac{\Lambda^{(d)}L^4R^3\Omega}{\mu^3|\vec{b}|^2}\sigma^2\right)^{-1} \tag{69}$$

Furthermore, by considering that the applied stress σ is usually in the range of MPa, terms multiplied by σ can be neglected in the further derivation because the terms involving A_e and μ are in the range of GPa. So, we obtain for P and Q

$$P = \left(\frac{1}{A_e} + \frac{2}{3}\frac{\Lambda^{(d)}L^2R\Omega}{\mu}\right)^{-1} \tag{70}$$

$$Q = \left(\frac{B_e}{A_e^3} - \frac{24}{5}\frac{\Lambda^{(d)}L^4R^3\Omega}{\mu^3|\vec{b}|^2}\sigma_0\right)\left(\frac{1}{A_e} + \frac{2}{3}\frac{\Lambda^{(d)}L^2R\Omega}{\mu}\right)^{-3} \tag{71}$$

If we use the nonlinearity parameter defined in equation (37), we can express β as

$$\beta = -\frac{Q}{P} = \frac{-\left(\frac{B_e}{A_e^3} - \frac{24}{5}\frac{\Lambda^{(d)}L^4R^3\Omega}{\mu^3|\vec{b}|^2}\sigma_0\right)}{\left(\frac{1}{A_e} + \frac{2}{3}\frac{\Lambda^{(d)}L^2R\Omega}{\mu}\right)^2} \tag{72}$$

By examining equation (70), it can be shown that the second term in the denominator is negligible compared to the first term, so we can simplify the nonlinearity parameter to

$$\beta = -\frac{B_e}{A_e} + \frac{24}{5}\frac{\Lambda^{(d)}L^4R^3\Omega A_e^2}{\mu^3|\vec{b}|^2}\sigma_0 \tag{73}$$

From this equation, we can easily distinguish the nonlinearity due to the nonlinear stress-strain relationship β^{lat} and dislocations β^{disloc}. As previously in section 2.4.1

$$\beta^{lat} = -\frac{B_e}{A_e} \tag{74}$$

therefore, the second term describes the contribution of dislocations and is dependent on parameters, like dislocation density $\Lambda^{(d)}$ and pinning distance of a dislocation $2L$.

$$\beta^{disloc} = \frac{24}{5}\frac{\Lambda^{(d)}LR^3\Omega A_e^2}{\mu^3|\vec{b}|^2}|\sigma_0| \tag{75}$$

The model, used to derive the contribution of dislocations on β, can be expanded to the stress initiated by precipitations if we consider an unconstraint precipitated particle with radius $r_0(1+\delta)$ inserted into a lattice structure with radius r_0. If we introduce the bulk modulus K of the precipitates, the shear modulus μ of the lattice and the actual misfit parameter ε, we obtain

$$r_p = r_0(1+\delta) \qquad \varepsilon = \frac{3K}{3K+4\mu}\delta \tag{76}$$

as derived by Martin [17].

A precipitate introduces a radial stress field $\sigma(r)$ in the lattice structure that can be written as

$$\sigma(r) = -\frac{4\mu\varepsilon r_p^3}{r^3} \tag{77}$$

If we evaluate the stress at the midpoint $r = \frac{L}{2}$, as shown in figure (4.8) [3], it yields

$$\sigma_0 = -\frac{64\mu\varepsilon r_p^3}{L^3} \tag{78}$$

which is the superposition of the two adjacent radial stress fields. By combining equation (75) and the local stress due to precipitations (equation (78)), we obtain β^{disloc} characterized by parameters of the dislocation and precipitated particles

$$\beta^{disloc} = 307.2\frac{\Lambda^{(d)} L^4 R^3 \Omega A_e^2 r_p^3}{\mu^3 |\vec{b}|^2}\frac{3K}{3K+4\mu}|\delta| \tag{79}$$

Like the Orowan stress (equation (51)), in practical applications the volume fraction f_p of precipitates is an important indicator for changes in the microstructure, and thus provides information about the stage of thermal aging. Consequently, Cantrell et al. [4] relate the radius of precipitates r_p and the average distance L between two precipitates to the volume fraction f_p by

$$L = \frac{2r_p}{\sqrt[3]{f_p}} \tag{80}$$

If we substitute equation (80) into (79), we come up with a far more elegant description of β^{disloc} since it is in terms of the volume fraction and radius of precipitates.

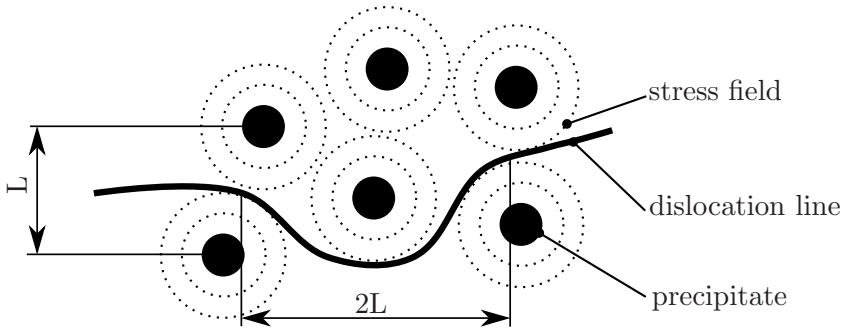

Figure 4.8: Bowing of dislocation line resulting from radial stress field of precipitates [4]

4.4.2 Evolution of the Nonlinearity Parameter β during Thermal Aging

The total nonlinearity consists of contributions by the lattice and the interaction of dislocations and precipitations. If we assume that β^{lat} remains constant for thermal aging and β^{disloc} changes as time passes, then the total nonlinearity parameter β changes with thermal aging and provides information on the microstructural evolution.

Dislocation density $\Lambda^{(d)}$, precipitation radius r_p and volume fraction f_p alter with aging time and can be related to the nonlinearity parameter by

$$\beta \propto \frac{\Lambda^{(d)} r_p^4}{\sqrt[3]{f_p}} \tag{81}$$

The resulting effects of equation (81) on β are summarized in table (4.3)

Table 4.3: Microstructural changes and their effects on β

Mechanism	Change in β	Comments
Dislocation density	$\Downarrow$	$\Lambda^{(d)}$ monotonically decreases
Nucleation	$\Downarrow$	many small precipitates r_p
Growth	$\Uparrow$	precipitate radius r_p and volume fraction f_p increases
Coarsening	$\Downarrow$	precipitate radius r_p increases, volume fraction f_p remains constant and precipitates lose their coherency

CHAPTER V

NONLINEAR ULTRASONIC MEASUREMENTS

The measurement setup, shown in figure 5.1, to generate and detect the nonlinear Rayleigh wave consists of an air-coupled transducer and a narrow band contact piezoelectric transducer, exciting a longitudinal wave. The exciting transducer is coupled to a plexiglas wedge, which is essential to generate the Rayleigh wave. A function generator is used to introduce a sinusoidal tone burst of 20 cycles at $2.1MHz$. To measure second harmonic waves in the specimen, we have to amplify the output signal of the function generator with the RITEC GA-2500A high power gated amplifier. The high-voltage signal travels as a Rayleigh wave along the surface and the air-coupled transducer receives the longitudinal acoustic wave that is leaked from the Rayleigh wave. The received signals are post-amplified to achieve a better signal-to-noise ratio, then recorded and averaged by the oscilloscope.

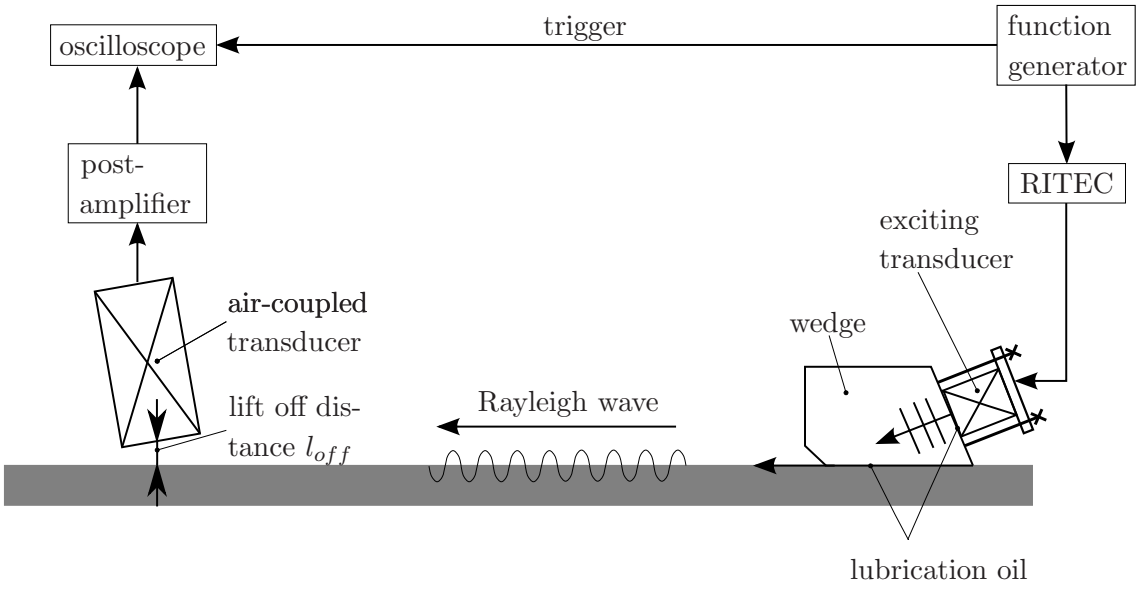

Figure 5.1: Experimental setup for nonlinear ultrasound measurements

5.1 Components

Detailed descriptions of the components are given in Thiele [24]. Thus, the purpose of this section is to give a summary of the key information and small adjustments made to ensure reliable results.

5.1.1 Function Generator

The function generator produces a tone-burst signal with a frequency of $2.1MHz$ and a peak to peak voltage of $800mV$. To ensure a sufficiently long steady state portion for the subsequent signal processing, we use an exciting signal containing 20 cycles.

5.1.2 High Power Amplifier

RITEC GA-2500A achieves the desired high-voltage excitation signal that is necessary to introduce waves with high acoustic energy, which is required to obtain a good signal-to-noise ratio for the significantly smaller component of the second harmonic. It emerges that a suitable gain factor for this type of amplifier is 7.4 (in the dial gauge) since any higher value deteriorates the signal or could even destroy the exciting piezoelectric transducer. It must be noted that the high power amplifier has to be turned on for at least 30 minutes before performing measurements. Otherwise, the device cannot guarantee a stable output signal, as shown by Walker [27].

5.1.3 Transducers

A Panametrics piezoelectric half inch narrow band transducer of type X is used to transform the electric input signal of the function generator into a longitudinal wave. We apply a frequency of $2.1MHz$ since the nominal frequency of the transducer is located at $2.25MHz$ and it is absolutely imperative that the excitation frequency is not the same as the nominal frequency.

The center frequency of the air-coupled transducer has to be close to the frequency of the second harmonic (around $4.2MHz$) to ensure the highest sensitivity. The air-coupled transducer converts the detected wave back to an electrical signal. In this study, an Ultran

NCT4-D13 with a nominal frequency of $4MHz$ and an active area of $12.5mm$ is used to detect the propagating waves (figure 5.2(b)).

5.1.4 Plexiglas Wedge

Theoretically, the generation of a Rayleigh wave is based on Snell's law that relates the geometry of the wedge (here angle θ_w) to the sound speeds of the wedge and the sample, c_D^{wedge} and c_R^{sample}, respectively. Snell's law can be written as follows

$$\theta_w = arcsin\left(\frac{c_D^{wedge}}{c_R^{sample}}\right) \tag{82}$$

where the wave speed c_D^{wedge} and c_R^{sample} can be obtained from the mechanical properties E, μ and ρ. As depicted in figure 5.2(a), by introducing a longitudinal wave into the wedge with a known wave speed c_D^{wedge} and Rayleigh velocity c_R^{sample} on the surface of the sample, we can determine the necessary angle θ_w to achieve a transformation from a longitudinal to a Rayleigh wave.

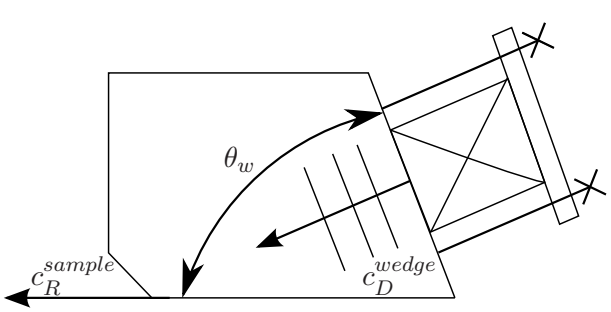

(a) Plexiglas wedge to transform longitudinal waves to Rayleigh waves

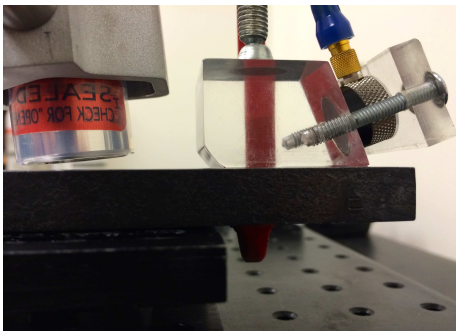

(b) Clamped wedge with exciting transducer and air-coupled transducer

Figure 5.2: Exciting transducer attached to wedge and receiving air-coupled transducer

Another factor that strongly affects the result of the measurement is the acoustic coupling condition achieved by light lubrication oil. The coupling condition is influenced by several factors, like the amount of oil, the clamping force and the surface condition of the sample. To achieve uniform results, it has to be ensured that all three boundary conditions are consistent in all measurements. Furthermore, time may be a relevant factor, since [27] observed a settling effect of the wedge. This phenomena is caused by the change of the thickness of the oil film, which slowly squeezes out over time. To meet this effect as well,

it is crucial to clamp the wedge to the sample at least 30 minutes before conducting the actual ultrasonic measurement. After this time, the influence due to settling is negligible and a stable coupling condition is accomplished.

5.1.5 Post-Amplifier

Further improvement of the signal-to-noise ratio is obtained by post-amplifying the signal of the air-coupled transducer with a Panametrics 5072PR pulser-receiver. Without amplification a lift off distance l_{off} (figure 5.1) of less than $2mm$ leads to a peak-to-peak voltage of approximately $1mV$, which is not usable for data acquisition with the oscilloscope. Therefore, the signal is enhanced by $40dB$ to obtain a measurable voltage of about $200mV$.

5.1.6 Acquisition of Data

Last component of the setup is the oscilloscope that records the amplified electrical output signal with an sampling rate of $250MS/s$ averaged over 256 sequences. Figure 5.3 shows a typical example for a signal averaged over 256 sequences in the time domain with a steady state portion, where a Hann window is applied [19], shown as red function. The purpose of the window is to remove the ringing effects in the beginning (voltage overshoot) and the end (ringing voltage).

The time domain signal has to be mapped to the frequency domain by applying fast Fourier transform (FFT). The resulting frequency spectrum is given in figure 5.4, where the contribution of the fundamental and second harmonic is clearly visible. However, we are not able to conclude from these voltage amplitudes to absolute particle displacement amplitudes in the material. Therefore, we have to introduce the electrical amplitudes A_1^{el} and A_2^{el}, which can be related proportionally to the nonlinearity parameter β.

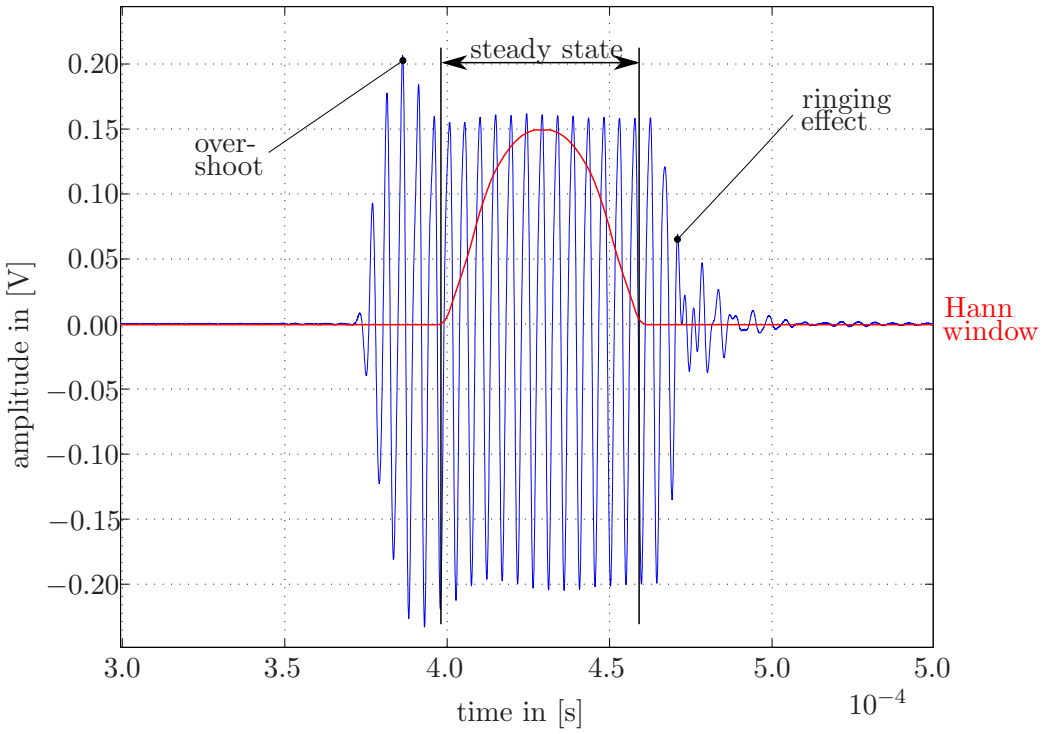

Figure 5.3: Typical output signal in time domain averaged over 256 burst and Hann window

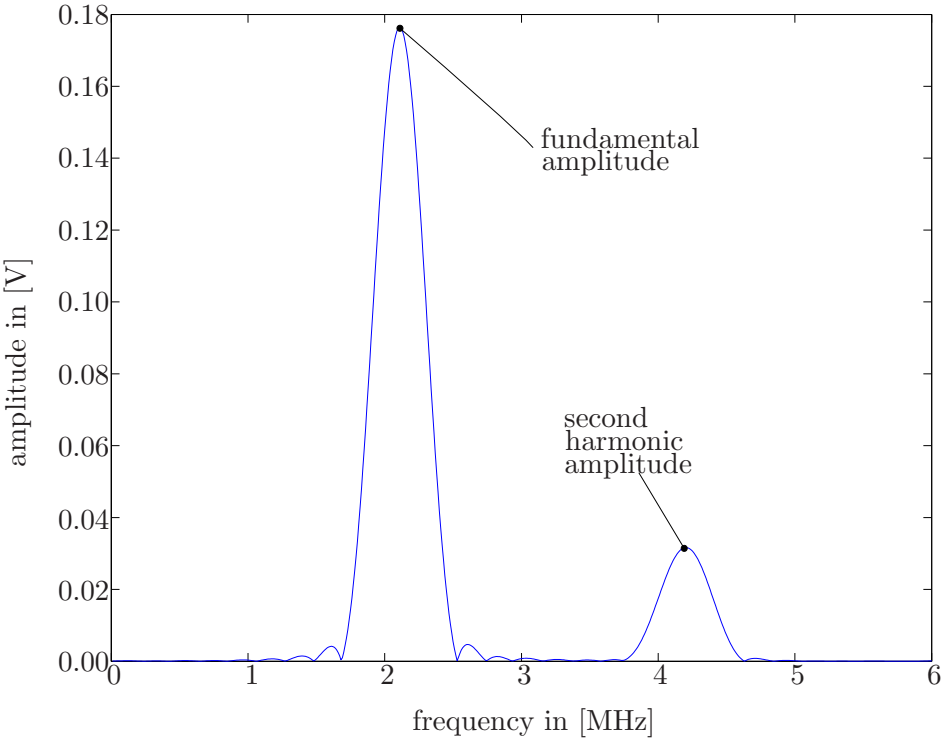

Figure 5.4: Typical output signal in frequency domain with A_1^{el} and A_2^{el}

5.2 Technical Approach to Measure Nonlinearity

The main goal of the technical approach is to minimize the influence of unwanted nonlinearities from the electrical system and other sources in the measurement system. The electrical components like transducer, amplifier and also the coupling condition introduce nonlinearity into the system that we are not interested in. Therefore, an increase in the excitation voltage, which means at the same time an increasing A_1^{el}, is not applicable, although the amplitude of the second harmonic increases. Figure 5.5(a) depicts the ideally linear relationship between the squared amplitude of the fundamental $(A_1^{el})^2$ and the amplitude of the second harmonic A_2^{el} wave, where the obtaining amplitudes are contributions of the amplifier, transducer, coupling condition and material nonlinearity. To simplify the graphical exposition of figure 5.5(a), we assume that all of the individual nonlinearities linearly change with an increase of $(A_1^{el})^2$. This leads to the problem that unwanted nonlinearities of amplifiers, transducers and coupling condition cannot be isolated from the material nonlinearity since the actual shares of the several nonlinearities in the total nonlinearity are unknown. Therefore, no statement about the material nonlinearity can be drawn.

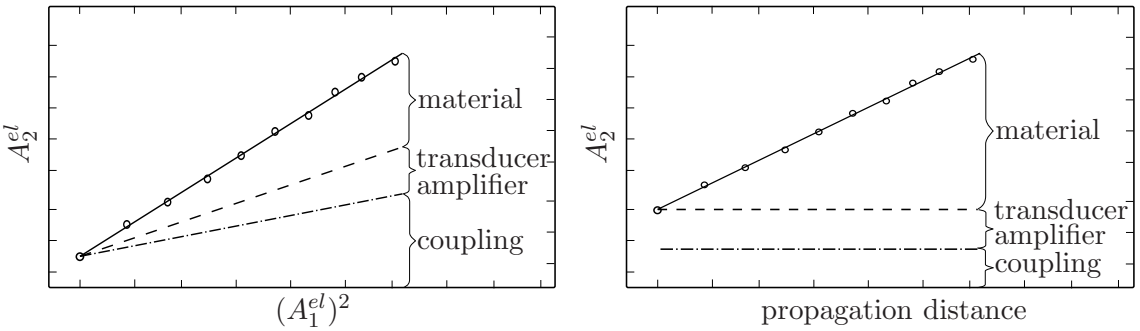

(a) Qualitative nonlinearity with increasing excitation voltage

(b) Qualitative nonlinearity with increasing propagation distance

Figure 5.5: Qualitative nonlinearity for an increasing excitation voltage and propagation distance

Instead of increasing the excitation voltage, we can change the propagation distance x_1 to determine the material nonlinearity since $A_2 \propto x_1$. The increase due to the change of the propagation distance can be explained by the energy transfer from the fundamental to the second harmonic. Theoretically, as depicted in figure 5.5(b), the nonlinearity due

to electrical devices stays at the same level for all measurements along the propagation distance. This allows a separation of unwanted nonlinearities and the material nonlinearity. However, this technical approach does not allow the performance of absolute measurements of β because of the following reasons:

1. Measured electrical amplitudes A_1^{el} and A_2^{el} still need to be related to the absolute particle displacement

2. Constant nonlinearity of transducers and amplifiers over propagation distance is unknown (figure 5.5(b))

3. Coupling condition, frequency response of transducer and lift off distance of air-coupled transducer influence A_1^{el} and A_2^{el}

It has to be noted that it is essential to ensure that the coupling condition, transducer and distance of the air-coupled transducer is always identical to guarantee comparable results among the measurements and the different specimens.

5.2.1 Assumptions to Process Ultrasonic Datas

So far, we assume that the propagating Rayleigh wave is a plane wave, where no diffraction happens and the nonlinearity parameter is proportional to $\frac{A_2}{A_1^2}$. This is not, however, the case for the three dimensional case, where diffraction and also attenuation influence the propagation of the wave. As a consequence, the nonlinearity parameter is not directly proportional to the ratio anymore. As Walker [27] and Thiele [24] previously examined, these effects are negligible for small propagation distances used, and thus a linear fitting can be applied to obtain the nonlinearity parameter β. The slope obtained by the linear fit is not equal to β, but it is proportional with a minimal influence of the unwanted nonlinearities. Thus, we have to introduce the relative nonlinearity parameter β' that results from the measured electrical output signal A_1^{el} and A_2^{el} of the transducer. For the relative nonlinearity parameter β' yields the following relationship

$$\beta' = \frac{A_2^{el}}{(A_1^{el})^2 x_1} \propto \frac{A_2}{A_1^2 x_1} \propto \beta \tag{83}$$

Since measurements with the absolute nonlinearity parameter β go beyond the scope of this study, we consider the relative parameter β' by evaluating the electrical contribution of the first and second harmonic wave A_1^{el} and A_2^{el}, respectively. This implies that all results are relative and are used to compare only the specimens measured under the same conditions. In the following the index "el" for the electrical first and second harmonic A_1^{el} and A_2^{el} will no longer be used since we set these amplitude proportional to β (this implies the proportionality to A_1 and A_2) and, furthermore, we measure exclusively in the relative regime.

Shull et al. [22] establish a model that accounts for diffraction and attenuation effects in the propagation of nonlinear Rayleigh waves, which is briefly summarized because it helps understand the trend of $(A_1)^2$ and A_2. By assuming that the wave field is generated by a line source of a Gaussian amplitude distribution, we can write the amplitude of the first harmonic as follows

$$A_1(x_1) = \frac{i\omega_1 A_{1,0} e^{-\alpha_1 x_1}}{\sqrt{1+\frac{ix_3}{\xi_1}}} e^{[i(k_1 x_1 - \omega_1 t - \varphi_{1,0})]} \tag{84}$$

where α_1 is the attenuation coefficient in x_1-direction and $\xi_1 = \frac{k_1 a_s^2}{2}$ with a_s as the radius of the Rayleigh wave source. Moreover, $A_{1,0}$ represents the initial first harmonic amplitude with the corresponding frequency and phase are indicated as ω_1 and $\varphi_{1,0}$, respectively. The interaction with nonlinearity sources lead to the generation of the second harmonic amplitude

$$\begin{aligned} A_2(x_1) = & -\frac{\sqrt{\pi}\beta\omega_1 A_{1,0}^2 k_1^2 a_s^2}{8c_R\sqrt{i(\alpha_2-2\alpha_1)(\xi_1+ix_1)}} e^{-\alpha_2 x_1 + i(\alpha_2-2\alpha_1)\xi_1} \\ & \left[erf\left(\sqrt{i(\alpha_2-2\alpha_1)(\xi_1+ix_1)}\right) - \right. \\ & \left. erf\left(\sqrt{i(\alpha_2-2\alpha_1)\xi_1}\right)\right] e^{[i(k_2 x_1 - \omega_2 t - \varphi_{2,0})]} \end{aligned} \tag{85}$$

with α_2 as the attenuation coefficient of the second harmonic amplitude. The expression "erf" indicates the Gauss error function and is defined as [2]

$$erf(x) = \frac{2}{\sqrt{\pi}} \int_0^x e^{-t^2}\, dt \tag{86}$$

To take account of the nonlinearity of the exciting transducer and the electrical system, we have to introduce the initial second harmonic $A_{2,0}^T$ that diffracts and attenuates along x_1.

It has the same mathematical expression as the fundamental amplitude in equation (84)

$$A_2^T(x_1) = \frac{i\omega_2 A_{2,0}^T e^{-\alpha_2 x_1}}{\sqrt{1+\frac{ix_1}{\xi_2}}} e^{[i(k_2 x_1 - \omega_2 t - \varphi_{2,0})]} \tag{87}$$

where ω_2 is the frequency and $\varphi_{2,0}$ the phase of the second harmonic. The summation of equation (85) and (87) leads to the amplitude of the second harmonic

$$|A_2(x_1)| = |A_2^M(x_1) + A_2^T(x_1)| \tag{88}$$

The unknown parameters α_1, α_2, $A_{1,0}$ and $A_{2,0}$ can be determined using the experimental results. This model of attenuation and diffraction of Rayleigh waves explains the trend of $(A_1)^2$ and A_2 over the propagation distance x_1 in figure 5.7.

5.2.2 Determination of the Acoustic Beam Path and Measurement along Propagation Direction

The exciting transducer is clamped to the wedge on the sample and by moving the air-coupled transducer in the x_1x_2-plane, we can perform a measurement of the first and second harmonic amplitudes along the propagation direction.

The angle between the air-coupled transducer and the surface of the specimen must be accurately adjusted to detect the leaked longitudinal wave. Theoretically, the angle can be calculated by using Snell's law but in practice an excited wave is used to find the true leak angle. We can modify the relative angle of the air-coupled transducer until the signal has the highest value (here at about 1.2°) for the electrical amplitudes, as depicted in figure 5.6(a). The relative angle is the value on the dial gauge and depends on the preceding adjustment by hand to find the area of the highest value.

In addition, according to Thiele [24] and experimentally observations, a determination of the acoustic beam path has to be carried out to find the propagation direction of the Rayleigh wave beam since the beam does not come straight out of the middle of the wedge. Not only an offset from the center but also an angle between the expected normal and actual beam direction can be observed.

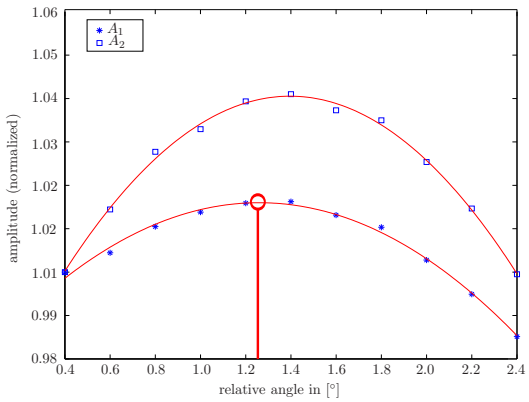

(a) Determination of acoustic path for the relative angle with a peak value at about 1.2°

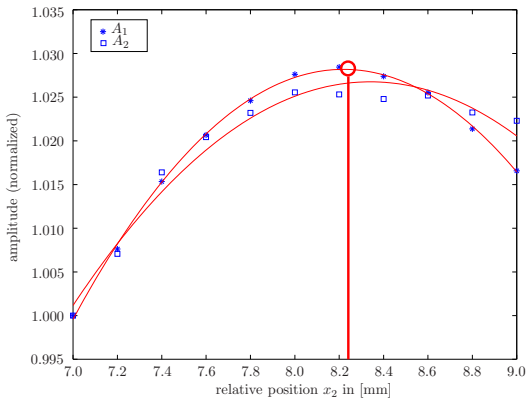

(b) Determination of acoustic path in the beginning ($x_1 = 25mm$) of the sample along x_2 with a peak value for A_1 at $8.25mm$ and A_2 at $8.35mm$

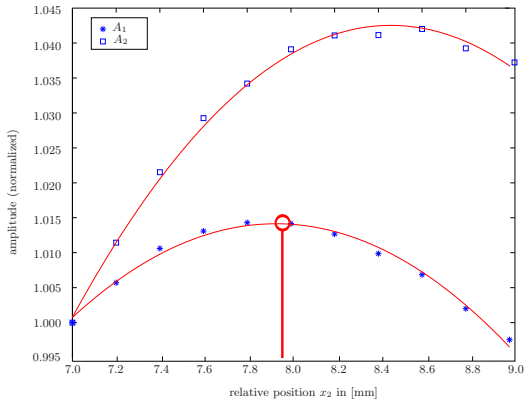

(c) Determination of acoustic path in the middle ($x_1 = 49mm$) of the sample along x_2 with a peak value for A_1 at 7.95 mm and A_2 at $8.35mm$

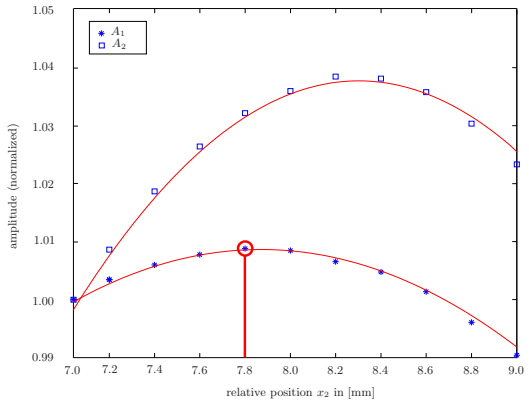

(d) Determination of acoustic path in the end ($x_1 = 71mm$) of the sample along x_2 with a peak value for A_1 at $7.80mm$ and A_2 at $8.25mm$

Figure 5.6: Typical determination of acoustic path with a frequency of $2.1MHz$ for the angle of the air-coupled transducer and the propagation distances $x_1 = 25mm$, $x_1 = 49mm$ and $x_1 = 71mm$

By measuring along the x_2-direction, we can state that the peak of A_1 and A_2 move from a relative x_2 position of $8.25mm$ and $8.35mm$ in the beginning ($x_{beg} = 25mm$), to $8.00mm$ and $8.35mm$ in the middle ($x_{mid} = 49mm$), up to $7.80mm$ and $8.25mm$ in the end ($x_{end} = 71mm$), as shown by figure 5.6(b-d). In some cases, the determination of the acoustic path reveals the problem that the peak of A_1 is not located at the same position as the peak of A_2. If this is the case, we determine that we always measure along the peak of the first harmonic amplitude to guarantee consistent results. Once we establish the actual path from the determination at 3 different distances, nonlinear measurements are performed along this predetermined path.

The air-coupled transducer can also move in the x_3-direction that changes the lift off distance l_{off}. However, to ensure comparable results it must always have the same distance from the surface of the specimen.

The actual measurement starts with adjusting a distance of $25mm$ between the wedge and the middle of the air-coupled transducer. This is followed by recording the value of A_1 and A_2 each $2mm$ along the predetermined propagation path. The 24 data points collected provide an increasing trend for A_2 and a decreasing trend for A_1, as depicted in figure 5.7(a). A_1 decreases almost monotonically with increasing propagation distance, which can be explained by the energy transfer taking place. Furthermore, attenuation and diffraction affect the fundamental amplitude and further enhance the decrease, as introduced by the model of Shull et al. [22]. As shown in figure 5.7(a), the nonlinear interaction leads to a monotonic increase of A_2 in the beginning of the measurements, and then levels off due to attenuation and diffraction, as also explained by the model in the previous section.

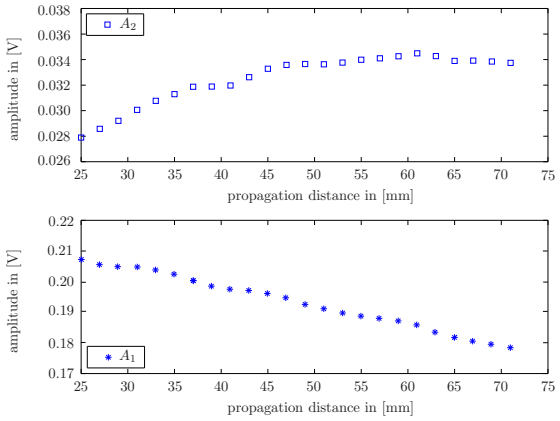

(a) Electrical amplitude A_1 and A_2 over the propagation distance x_1

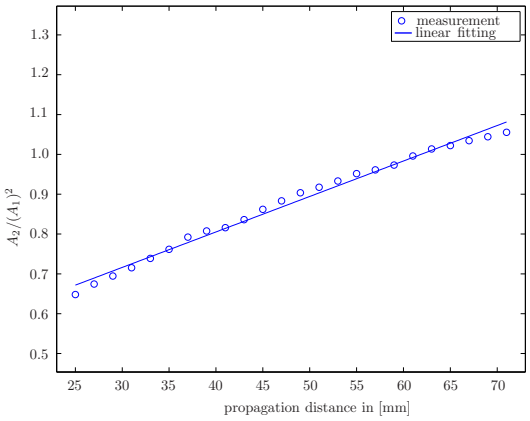

(b) Ratio A_2 over $(A_1)^2$ over the propagation distance x_1

Figure 5.7: Typical results for a measurement with a frequency of $2.1MHz$ for sample 1 (untreated sample)

Figure 5.7(b) delineates the ratio A_2/A_1^2 where the slope of the linear fit represents the relative nonlinearity parameter β'. Chapter 6 provides more detailed information on the results achieved for each sample. It has to be noted that for each measurement 24 measurement points (propagation path up to $71mm$) are used for the linear fit.

CHAPTER VI

EXPERIMENTAL RESULTS AND INTERPRETATION

In addition to the above mentioned nonlinear ultrasonic measurements, hardness tests and a scanning electron microscopy (SEM) are conducted for each specimen to provide sufficient information on the microstructure. This chapter summarizes the results obtained from each test, followed by an interpretation to establish a relationship between the nonlinearity parameter β' and the microstructure.

6.1 Complementary Measurements

The scanning electron microscopy (SEM) is performed with a JOEL JSM-7600F microscope. Furthermore, element mapping and energy dispersive X-ray microanalyses (EDX) are conducted to emphasize the distribution and concentration of the three more important alloying elements chromium, molybdenum and iron.

Additionally, Rockwell hardness test for each specimen is conducted to receive information about the progress of the mechanical properties.

6.1.1 Scanning Electron Microscopy Results

To obtain the metallographic results, the specimens are carefully ground with emery paper to a grade of 1200 and subsequently polished with a $1\mu m$ diamond solution and cloth. The microstructure is revealed using a Villela's reagent, which is a common metallographic etchant for heat treated steels and martensitic stainless steels. It contains $100ml$ ethanol, $5ml$ HCl and $1g$ of picric acid.

Figure 6.1(a-l) shows the sequence of the SEM images which is completed by the corresponding element mapping that indicates the distribution of the three more important alloying elements Fe, Cr and Mo. The number 1, 2, 3 and 4 marks the position, where energy-dispersive X-ray spectroscopy (EDX) is applied to determine the element concentration (table 6.1).

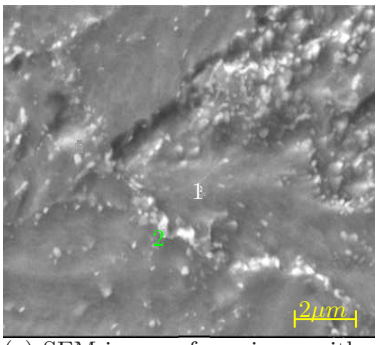

(a) SEM image of specimen with a holding time of $0h$

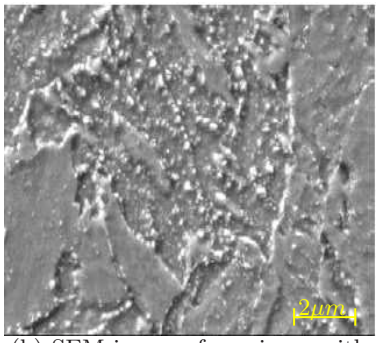

(b) SEM image of specimen with a holding time of $200h$

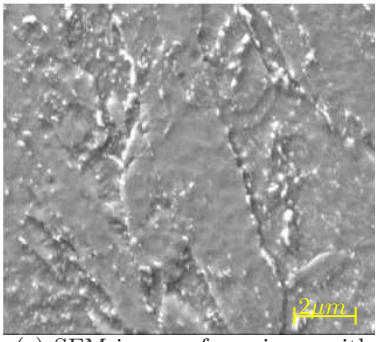

(c) SEM image of specimen with a holding time of $500h$

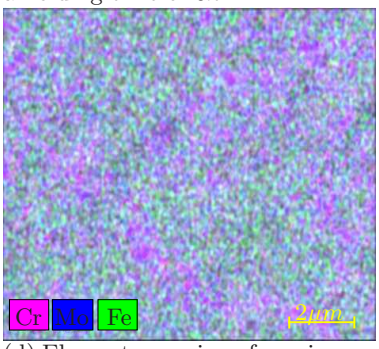

(d) Element mapping of specimen with a holding time of $0h$

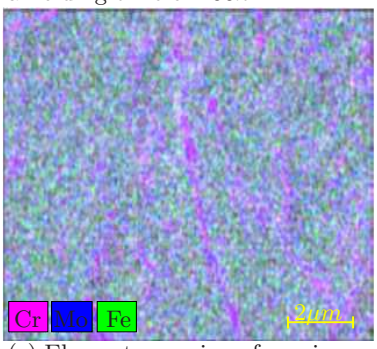

(e) Element mapping of specimen with a holding time of $200h$

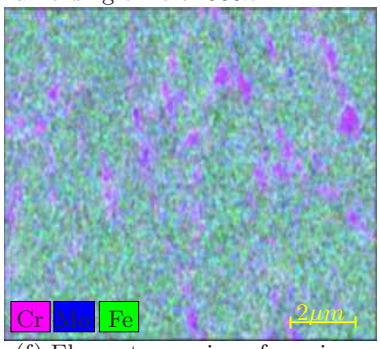

(f) Element mapping of specimen with a holding time of $500h$

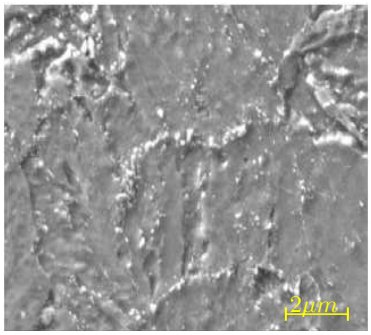

(g) SEM image of specimen with a holding time of $1000h$

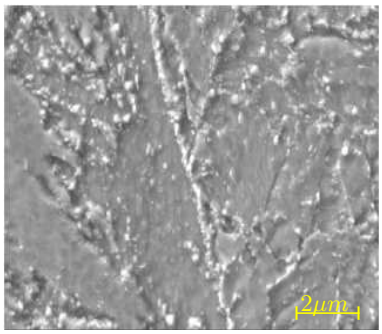

(h) SEM image of specimen with a holding time of $1500h$

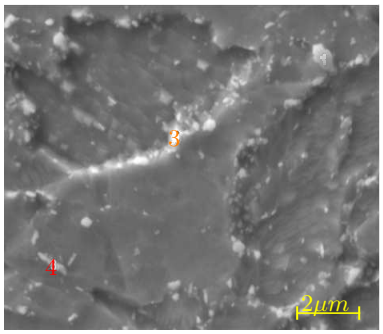

(i) SEM image of specimen with a holding time of $3000h$

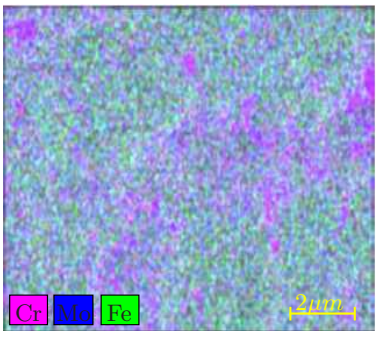

(j) Element mapping of specimen with a holding time of $1000h$

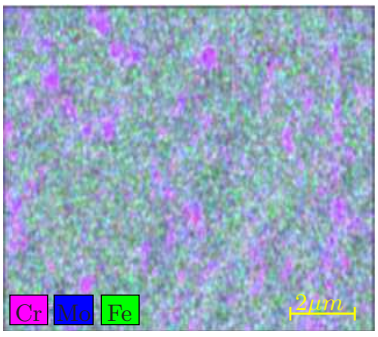

(k) Element mapping of specimen with a holding time of $1500h$

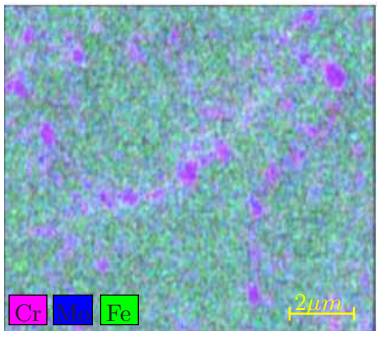

(l) Element mapping of specimen with a holding time of $3000h$

Figure 6.1: SEM image (a-c, g-i) and element mapping (d-f, j-l) of all specimens

We determine the element concentration of the matrix and an arbitrary particle for the untreated specimen, and furthermore two arbitrary precipitated particles for the specimen with a holding time of $3000h$.

In general, the precipitation sequence depends mainly on the composition of the steel but the diffusivities of the alloy elements and the ease of nucleation are also important considerations determining the favored carbide phases [28].

Initially, particles are seen to be evenly distributed in the matrix and at the boundary of grains. As can observed in figure 6.1(b), iron (green) and molybdenum (blue) are homogeneously distributed, whereas chromium (purple) shows a higher concentration in some areas, however, it still has some level of regularity in its distribution. The element mapping also reveals that prior to heat treatment the particle radius $r_p << 1\mu m$. Table 6.1 represents the element concentration of two particles and the matrix for the specimen with a holding time of $0h$ and $3000h$.

As aging time progresses, the diffusion of chromium forms bigger particles located at sub-grain boundaries and at former austenite grain boundaries [9], as depicted in figure 6.1(l). Particularly the chromium and molybdenum particles gather and create areas with a higher chromium content, as evidenced by the element concentration of the particles in table 6.1.

The chromium concentration after $3000h$ holding time is almost three times higher as in the untreated specimen. Expressed in numbers, if we compare the precipitated particle (2) with the precipitated particle (3), an increases from 11.2% to 29.1% is observable, leading to a sharp decline of the iron concentration from 70.1% to 42.3%. From table 6.1, we can also see that all precipitated particles are richer in carbon (8.8%), chromium (11.2%) and molybdenum (0.9%) than the matrix (1), which consequently results in the assumption that the particles may be a chromium carbide type. Vitek [26] also investigates the precipitation of chromium carbides. Furthermore, the particle size increases for each further aged specimen and after $3000h$ particles reach a size of about $1\mu m$ in diameter.

Table 6.1: Element concentration for specimen with $0h$ (matrix (1) and particle (2)) and for specimen with $3000h$ (particle (3) and particle (4))

Element	[wt. %] matrix (1)	[wt. %] particle (2)	Element	[wt. %] particle (3)	[wt. %] particle (4)
Iron	82.1	70.1	Iron	42.3	48.7
Carbon	4.4	8.8	Carbon	11.3	8.7
Chromium	**7.0**	**11.2**	**Chromium**	**29.1**	**26.4**
Vanadium	2.3	1.9	Vanadium	3.3	3.1
Molybdenum	0.5	0.9	Molybdenum	0.3	0.1
Silicon	0.3	0.3	Silicon	0.1	0.2

6.1.2 Hardness Results

A clear decrease of hardness with increasing holding time is observed in figure 6.2 for the heat treated specimens. The modified 9%Cr steel indicates an initially drastic decrease up to a holding time of $500h$. The averaged value drops from $22.5HRC$ to $19.8HRC$ within $500h$. After that time, the hardness gradually reduces to a value of $18.5HRC$.

A similar trend of rapid decrease, followed by a slight decrease in the hardness are reported by Wendell [28], who investigates the behavior for different temperatures and has found out that with increasing temperature the initial slope becomes steeper. These findings correlates to the behavior of the dislocation density in section 4.2.2, which has the same trend for an increasing temperature.

This correlation can be explained with the characteristic of the hardness. At the beginning of the thermal aging process, the high amount of lath martensite dissolutes containing a high dislocation density $\Lambda^{(d)}$. Consequently, the decrease of $\Lambda^{(d)}$ is at first high and slows down since as time passes there is less lath martensite to dissolute.

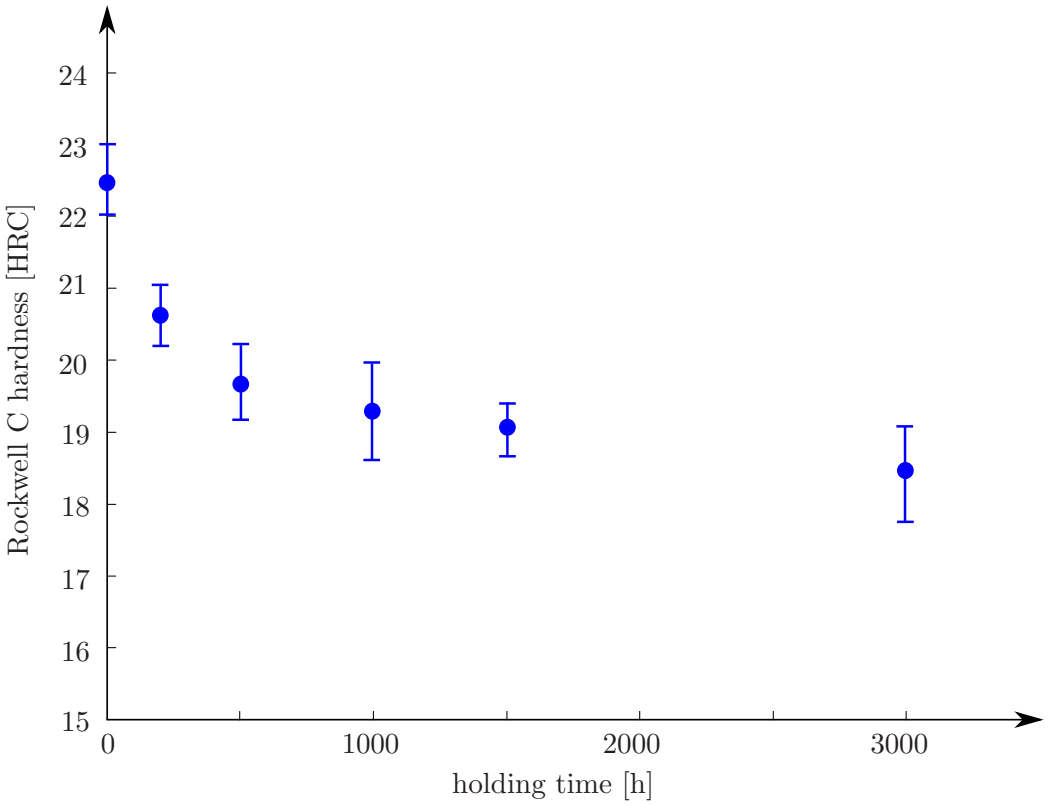

Figure 6.2: Rockwell C hardness of the specimens over holding time

6.2 Nonlinear Ultrasonic Results

The nonlinear ultrasonic measurements are conducted as described in chapter 5. We perform at least 10 measurements for each specimen; one measurement consists of the determination of the acoustic beam path and the actual measurement along the predetermined path. In figure 6.3, the relative nonlinearity parameter β', normalized by the mean value of the untreated specimen, is plotted over the aging time in hours. The error bar indicates the maximal variation of the results for each specimen. The maximal error was 10% for the last specimen, which is still an acceptable value for a nondestructive evaluation purpose.

Figure 6.3 shows an initially rapid decrease of β' followed by an increase after the aging time of $500h$. In the first $500h$ drops the nonlinearity parameter from 100% to about 70%. This drop of 30% can be explained by the reduction of the dislocation density. The further increase up to $3000h$ is reasonable because the precipitated particles start to grow and after $3000h$ the nonlinearity parameter β' reaches a value of 113% compared to the base sample.

At some point the structure coarsens because the large particles grow at the expense of the small ones resulting in a decrease of the nonlinearity parameter β'.

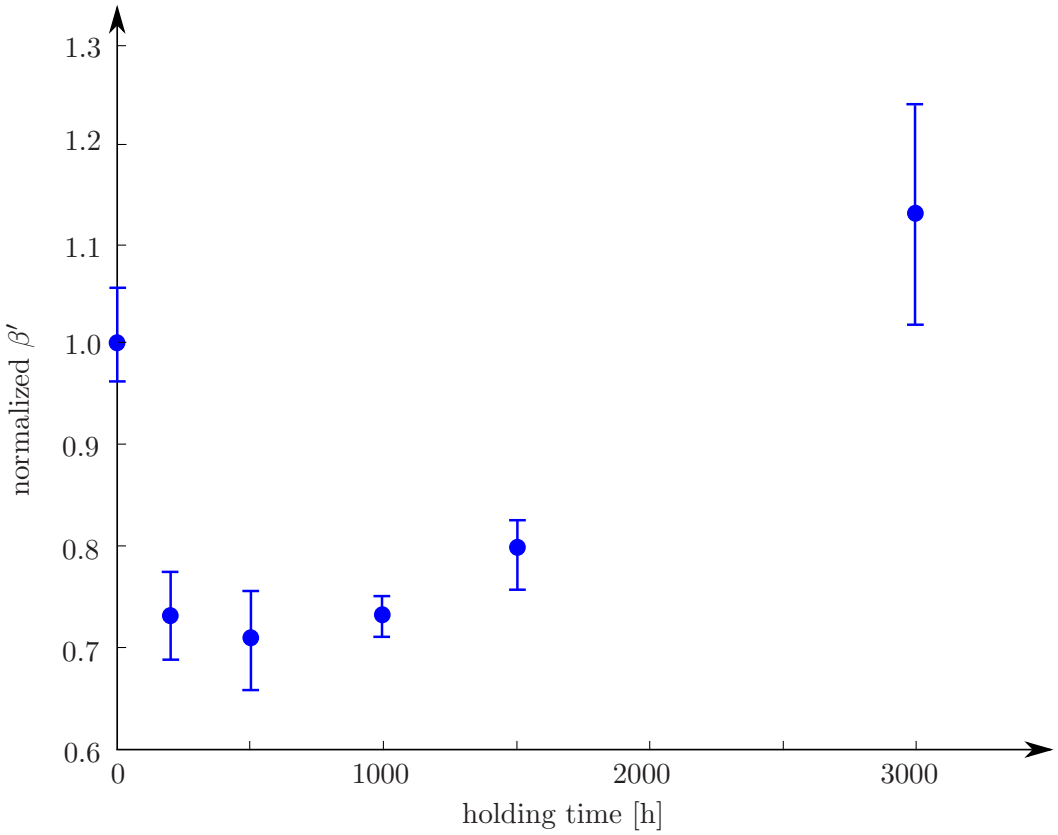

Figure 6.3: Relative nonlinearity parameter β' averaged by the mean value of the untreated sample over holding time

With the significant changes of β', we can conclude that the nonlinearity parameter is very sensitive to the microstructural evolution including dislocations and precipitations. This trend is supported by Park et al. [20] who also measure the nonlinearity parameter for a 10.5%Cr steel with a different composition of alloying elements. They investigate this material for several aging temperatures and results of the nonlinearity parameter show a similar trend as the results in figure 6.3.

Figure 6.3 can be subdivided into an initial phase dominated by decreasing contributions and a second phase dominated by increasing contributions on β'. Up to an aging time of $500h$ the decrease in second harmonic generation might be caused by the reduction of dislocations and the precipitate nucleation process. This phase is followed by an increasing

phase, where the growth of precipitated particles predominates. However, this hypothesis needs to be further investigated since the quantitative effect of dislocations and precipitated particles on β' has not been finally clarified. Furthermore, as explained in section 4.2.2, the interaction between dislocation and precipitates is very complicated and a more precise insight into the microstructural evolution is necessary including the determination of the dislocation density $\Lambda^{(d)}$, the exact size of the particles r_p and their volume fraction f_p.

6.3 Comparison of the Results

This section compares the nonlinear measurements obtained with the air-coupled transducer to the complementary measurements. As previously mentioned the nonlinearity parameter can be divided in two phases, as depicted in figure 6.4.

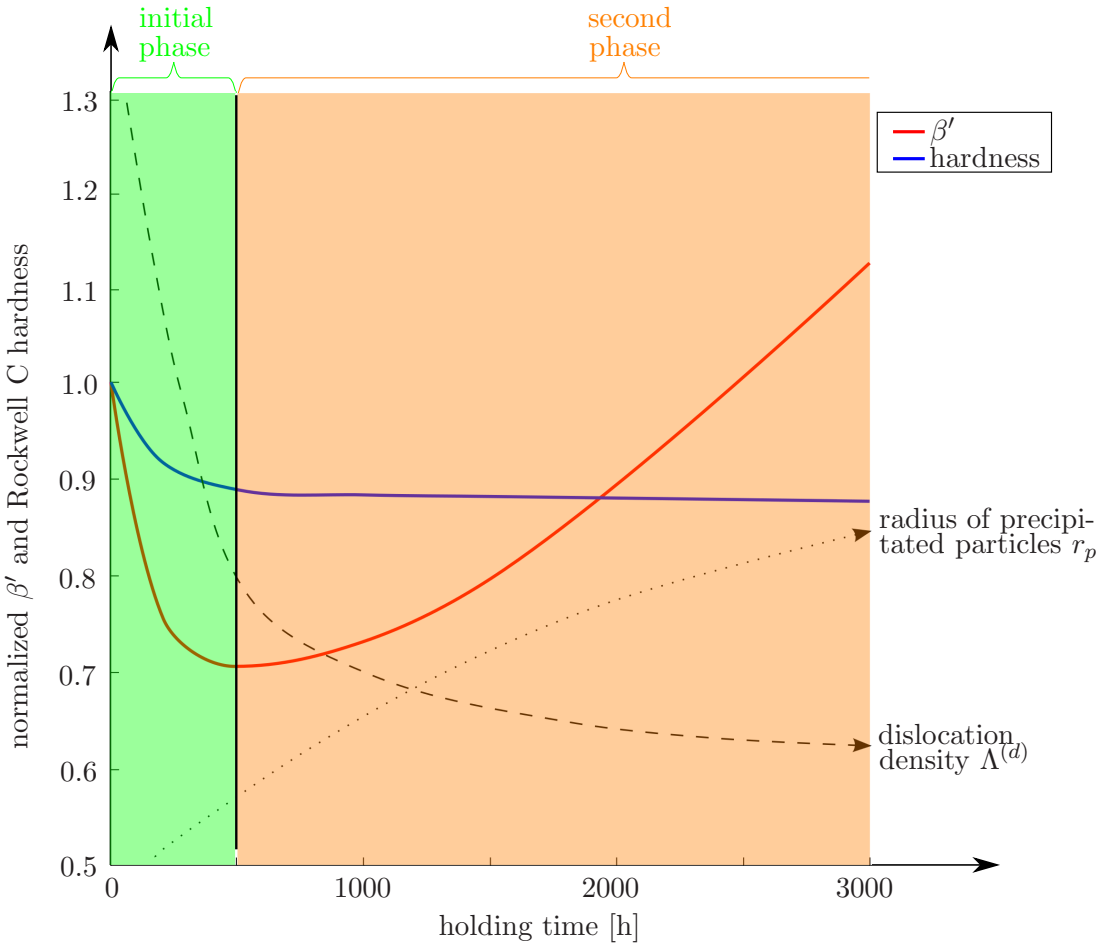

Figure 6.4: Comparison of hardness and ultrasonic results with the qualitative trend of the dislocation density and radius of precipitated particles

Again the nonlinearity parameter β' and the Rockwell C hardness is averaged by the mean value of the untreated sample. The qualitative curve of the dislocation density (dashed line) and the radius of precipitated particles (dotted line) is extracted from other studies on similar steels ([20], [21] and [5], [6], [11] respectively).

The initial phase clearly shows a simultaneous decrease in the hardness and nonlinearity parameter. One can qualitatively see that in this phase the dislocation density $\Lambda^{(d)}$ drops significantly and at the same time the radius of the precipitated particles r_p increases. From the characteristic of β' and hardness, we can conclude that the microstructural change associated with the dropping dislocation density is the dominating mechanism.

The second phase indicates a proceeding slight decrease in the hardness, whereas the nonlinearity parameter climbs again after passing the minimum at $500h$. It even exceeds for an aging time of $3000h$ the starting value by approximately 13%. In this phase the reduction of $\Lambda^{(d)}$ flattens and simultaneously the earlier nucleated particles grow in size. The results obtained imply that the second phase is probably dominated by the contribution of the growing precipitates.

CHAPTER VII

CONCLUSION AND OUTLOOK

This study investigates isothermally aged ferritic martensitic steel using nonlinear Rayleigh surface waves. Rayleigh waves are generated with the contact wedge method and detected by an air-coupled transducer. To obtain the relative nonlinearity parameter β', the propagation distance is varied by moving the air-coupled transducer along a line in the propagation direction. This procedure allows a decoupling of the system nonlinearity and the desired material nonlinearity. However, this procedure only measures relative values of nonlinearity, because the quantitative correlation between the measured electrical output signal from the air-coupled transducer and the absolute amplitude of the propagating wave has not yet been determined. Furthermore, the nonlinearity from the coupling condition and the contribution from the electronic devices are not yet fully quantified.

Additionally, background information on the generation of the second harmonic due to dislocations and precipitated particles is provided, since these microstructural changes are indicators for the thermal aging process. A brief summary of the most common precipitations and the mechanism during thermal aging is given to enable the interpretation of the nonlinear results obtained. Finally, complementary measurements are conducted to explain and support the nondestructive investigation.

A heat treatment schedule with various holding times is performed to obtain a sequence of heat treated 9%Cr ferritic martensitic steels. The nonlinear ultrasonic results indicate an initially rapid decrease in the generation of the second harmonic, followed by an increase in the nonlinearity parameter β'. The initial phase is dominated by decreasing material nonlinearity contributions from the microstructure like the decrease of dislocation density. As the second phase starts, the reduction of the dislocation density slows down and increasing material nonlinearity contributions such as the growth of precipitated particles becomes the decisive influence, which causes the measured increase in β'.

The scanning electron microscopy and hardness measurements support the results obtained by the nonlinear ultrasonic measurements. The monotonic decrease in hardness serves as an indicator for the decrease of the dislocation density since the curve of the hardness can be described by the dissolution of lath martensite that contains a high dislocation density. Furthermore, the scanning electron microscopy reveals the growth of the precipitated particles as the aging process progresses. The untreated specimen contains small, evenly distributed chromium containing precipitates. SEM images show that the further the aging process advances, the bigger the precipitates are.

The nonlinearity parameter β' provides an understanding of, and information on the microstructure and hardness. However, for an absolute assessment, one needs to develop a quantitative model that describes this evolution process and the corresponding changes in β'.

Further work needs to be done to investigate the performance of the air-coupled transducer in terms of determining the peaks of the acoustic energy. Studies have shown that the peak value of the first and second harmonic amplitude may not always lie on top of each other. In this context, it is also important to examine more closely the reasons for the offset and the path of the acoustic energy.

Moreover, an investigation of smaller samples with the air-coupled transducer has revealed problems with possible interferences from the edges. This problem can be analyzed by using different sized samples and describe the influence of the size on the amplitudes measured.

As soon as the reliability of the air-coupled transducer is assured, further work can be done to completely characterize the correlation between the second harmonic generation and the microstructural evolution. To find an appropriate model, which describes the contribution of precipitated particles and dislocation density on the nonlinearity parameter, it is inevitable to gather more accurate data including the dislocation density, the exact size and type of the precipitated particles for each stage of thermal aging. These data allow a more quantitative evaluation of the changing nonlinearity parameter β.

Finally, samples with a longer holding time would be an interesting addition to the already existing study, to monitor the further progress of the aging process up to the point of a visible damage. Also, samples with a different amount of chromium would be interesting and helpful to understand the microstructural evolution in this class of materials.

REFERENCES

[1] Achenbach, J. D., *Wave Propgation in Elastic Solids*. Amsterdam: North-Holland Pub. Co., 1973.

[2] Andrews, L. C., *Special functions of mathematics for engineers*. New York: SPIE Press and Oxford University Press, 1998.

[3] Cantrell, J. H. and Yost, W. T., "Nonlinear ultrasonic characterization of fatigue microstructures," *International Journal of Fatigue*, vol. 23, no. 1, pp. 487 – 490, 2001.

[4] Cantrell, J. H. and Zhang, X.-G., "Nonlinear acoustic response from precipitate-matrix misfit in a dislocation network," *Journal of Applied Physics*, vol. 84, pp. 5469 – 5472, 1998.

[5] Cipolla, L. and Materiali, C. S., "Microstructural evolution during creep tests of 9% steel grades," *Eighth International Conference on Creep and Fatigue at Elevated Temperatures*, 2007.

[6] Danielsen, H. K. and Hald, J., "Influence of z-phase on long-term creep stability of martensitic 9 to 12 % cr steels," *VGB Power Tech*, vol. 5, pp. 68 – 73, 2009.

[7] Danielsen, H. K., *Z-phase in 9-12%Cr Steels*. PhD thesis, Department of Manufacturing, Technical University of Denmark, 2007.

[8] Deschepper, M. and Filee, J., "Industeel groupe arcelor," no. 372758, 2005.

[9] Eggeler, G., "The effect of long-term creep on particle coarsening in tempered martensite ferritic steels," *Acta metall*, vol. 37, no. 12, pp. 3225 – 3234, 1989.

[10] Guo, Z. and Sha, W., "Quantification of precipitation hardening and evolution of precipitates," *Materials Transaction*, vol. 43, no. 6, pp. 1273 – 1282, 2002.

[11] Hald, J., "Microstructure and long-term creep properties of 912% cr steels," *Pressure Vessels and Piping*, vol. 85, pp. 30 – 37, 2008.

[12] Hamilton, M. F. and Blackstock, D. T., *Nonlinear Acoustics*. Academic Press, 1998.

[13] Herrmann, J., Kim, J.-Y., Jacobs, L. J., Qu, J., Littles, J. W., and Savage, M. F., "Assessment of material damage in a nickel-base superalloy using nonlinear rayleigh surface waves," *Journal of Applied Physics*, vol. 99, no. 12, 2006.

[14] Hikata Akira, B. B. C. and Elbaum, C., "Dislocation contribution to the second harmonic generation of ultrasonic waves," *Journal of Applied Physics*, vol. 36, no. 1, pp. 229 – 236, 1965.

[15] Hull, D. and Bacon, D., *Introduction of Dislocations*. Liverpool: Elsevier, 2011.

[16] Jablonski, P. D., "9cr-1 mo steel material for high temperature application," *United States Patent*, no. Patent N0.2 US 8,317,944 B1, 2012.

[17] Martin, J. W., *Precipitation Hardening*. Butterworth Heinemann, 1998 2nd edition.

[18] Nabarro, F., "The statistical problem of hardening," *Journal of the less common metals*, vol. 28, no. 2, pp. 257 – 276, 1972.

[19] Oppenheim, A. V. and Schafer, R. W., *Discrete-time signal processing*. Upper Saddle River, NJ: Prentice Hall, 1999.

[20] Park Jaeseok, K. M., "Correlation of metallurgical analysis and higher harmonic ultrasound response for long term isothermally aged and crept fm steel for usc tpp turbine rotors," *NDT&E International*, no. 54, pp. 159 – 165, 2013.

[21] Sawada Kota, K. M., "Contribution of microstructural factors of hardness change during creep exposure in mod.9cr-1mo steel," *ISIJ International*, vol. 45, no. 12, pp. 1934 – 1939, 2005.

[22] Shull D. J., Kim E.E., Z. E. A., "Diffraction effects in nonlinear rayleigh wave beams," *Journal of the Acoustical Society of America*, vol. 97, no. 4, pp. 694 – 2137, 1995.

[23] Strang, A. and Vodarek, V., "Z phase formation in martensitic 12crmovnb steel," *Materials and Science Technology*, vol. 12, pp. 552 – 556, 2007.

[24] Thiele, S., "Air-coupled detection of rayleigh surface waves to assess material nonlinearity due to precipitation in alloy steel," Master's thesis, Georgia Institute of Technology, 2013.

[25] Viktorov, I. A., *Rayleigh and Lamb waves: physical theory and applications*. New York: Plenum Press, 19673.

[26] Vittek J. L., R. L. K., "Precipitation reactions during the heat treatment of ferritic steel," *Metallurgical Transactions*, vol. 14, pp. 1047 – 1055, 1983.

[27] Walker, S., "Fatigue damage evaluation in a36 steel using nonlinear rayleigh surface waves," Master's thesis, Georgia Institute of Technology, 2011.

[28] Wendell B. Jones, C. R. Hills, D. H. P., "Microstructural evolution of modified 9cr-1mo steel," *Metallurgical Transactions*, vol. 22, pp. 1049 – 1058, 1991.

[29] Yao Q., S. J., "First-principles studies of defects, mechanical properties and electronic structure of cr-based laves phases," *Intermetallics*, no. 15, pp. 694 – 699, 2007.

[30] Zabolotskaya, E., "Nonlinear propagation of plane and circular rayleigh waves in isotropic solids," *Acoustical Society of America*, 1992.

[31] Zeitvogel, D., "Characterization of damage due to stress corrosion cracking in carbon steel using nonlinear rayleigh surface acoustic waves," Master's thesis, Georgia Institute of Technology, 2012.